performed. Differences at the 95% confidence level ($P<0.05$) were considered significant.

Results

Characterization of Bt-PAMAM-DTPA(Gd)

Bt-PAMAM-DTPA(Gd) was synthesized in four steps from PAMAM in a yield of 63%. PAMAM was conjugated to 9.9±1.3 biotins and 43.6±1.9 DTPAs, which were quantitatively coordinated to Gd. Bt_1-PAMAM-DTPA(Gd) containing 1.0±0.1 biotin and 47.6±2.2 DTPAs on PAMAM dendrimer was also synthesized. The ^{153}Gd-labeled Bt-PAMAM-DTPA(Gd), which was incubated with mouse plasma for 24 h, did not release any low molecular weight metabolites or free radiometals (Fig. 1).

The competitive binding assay revealed that all of the contrast agents inhibited the binding of ^{125}I-IBB to streptavidin in a dose-dependent manner (Fig. 2). The IC_{50}s for Bt-PAMAM-DTPA(Gd), Bt_1-PAMAM-DTPA(Gd), and D-biotin were 32±31, 1,390±1,220, and 60±45 nM, respectively, demonstrating that Bt-PAMAM-DTPA(Gd) had about 1.9- and 43.2-fold higher affinity to streptavidin than D-biotin and Bt_1-PAMAM-DTPA(Gd).

MR Imaging Study (Phantom Study)

The *in vitro* T_1-weighted MR images with Bt-PAMAM-DTPA(Gd) and Gd-DTPA are shown in Fig. 3a. Water and PBS were used as baselines. With the same Gd concentration, the signals with Bt-PAMAM-DTPA(Gd) were higher compared to Gd-DTPA. The longitudinal relaxation rate ($1/T_1$) *vs.* the concentration of Gd for both contrast agents are shown in Fig. 3b with good linear fits ($R^2=1.00$ and 0.99 for Bt-PAMAM-DTPA(Gd) and Gd-DTPA, respectively). Calculated $r1$ values (L mmol^{-1} s^{-1}) for Bt-PAMAM-DTPA(Gd) and Gd-DTPA were 15.5±1.1 and 3.6±0.1, respectively, which shows that the proton relaxivity of Bt-PAMAM-DTPA(Gd) was 4.3-fold higher than that of Gd-DTPA ($P<0.0001$).

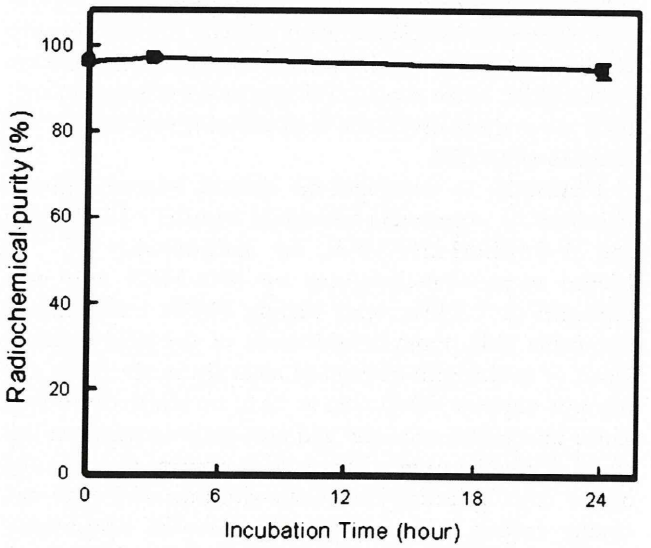

Fig. 1. Size exclusion analysis of ^{153}Gd-labeled Bt-PAMAM-DTPA(Gd) radioactivity after incubation at 37°C in mouse plasma. The *error bars* represent standard deviations.

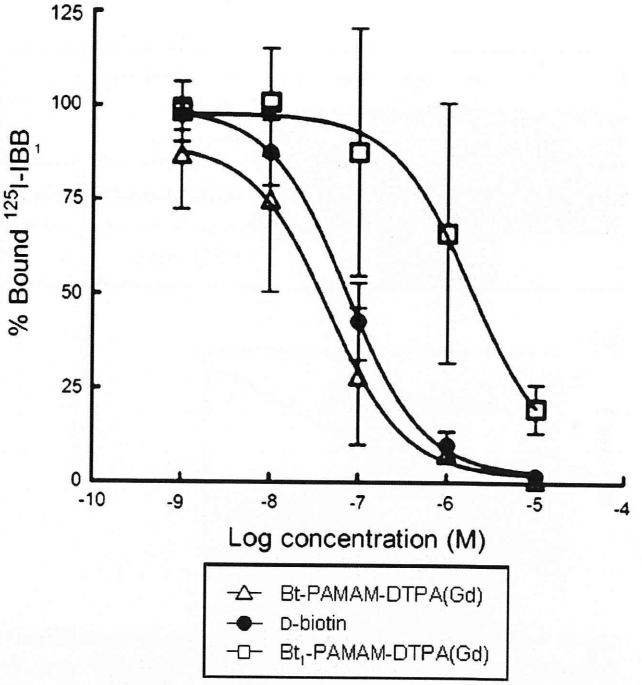

Fig. 2. Inhibition of ^{125}I-IBB binding to streptavidin by D-biotin, Bt-PAMAM-DTPA(Gd), or Bt_1-PAMAM-DTPA(Gd).

MR Imaging Study (In Vivo Study)

Fig. 4a (coronal) and b (transaxial) show *in vivo* T_1-weighted MR images of tumor-bearing mice before and at 5 and 180 min after injection of Bt-PAMAM-DTPA(Gd) following pre-treatment with streptavidin-conjugated anti-MT1-MMP mAb (MT1-MMP), streptavidin-conjugated negative control IgG (negative control), or saline (saline). In the MT1-MMP group, the most intense signal was observed in the margin of the tumor, as compared with the tumor core, over the 180-min period. The relative signal intensity (rSI) in the tumor and the relative T/M ratio were strongly enhanced just after administration of Bt-PAMAM-DTPA(Gd) and were highly maintained for 3 h after the contrast agent injection which displayed rapid clearance from the circulation (Fig. 4c, d). These signals were significantly greater than those from the negative control group ($P<0.05$ (at 44 and 55 min), $P<0.01$ (at 2 and 3 h)). In the saline group, Bt-PAMAM-DTPA(Gd) readily disappeared from the circulation and mainly accumulated in the kidneys. Though the relative signal intensity in the tumor also increased

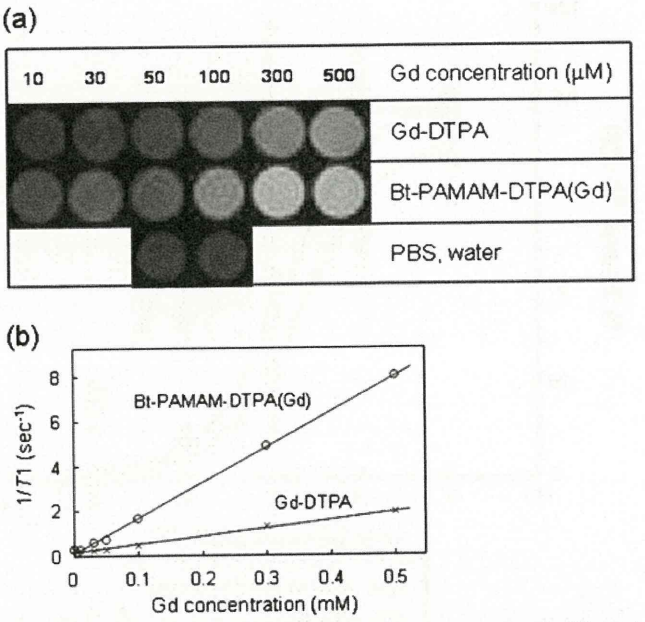

Fig. 3. **a** *In vitro* T_1-weighted MR measurements of different concentrations of Gd (micromolar) from Gd-DTPA and Bt-PAMAM-DTPA(Gd) in PBS at 1.5 T. PBS and water were used as references. These images show that at all concentrations, the signals are greater for Bt-PAMAM-DTPA(Gd) than for Gd-DTPA. **b** Longitudinal relaxation rate ($1/T_1$) *vs.* the concentration of Gd from Gd-DTPA (*crosses*) and Bt-PAMAM-DTPA (Gd) (*circles*) in PBS at 1.5 T are presented with good linear fits (R^2>0.99). The *r*1 value for Bt-PAMAM-DTPA(Gd) was 4.3-fold higher than for Gd-DTPA.

(190%) just after administration of Bt-PAMAM-DTPA(Gd), it decreased to the basal level (115%) within 3 h (Fig. 4c). A slightly higher tumor signal was obtained in the negative control group than in the saline group only 3 h after injection of Bt-PAMAM-DTPA(Gd) (P<0.01). The time-dependent change of relative T/M ratios was similar to that of the relative signal intensity in the tumor (Fig. 4d). The time-dependent change of relative signal intensity in the kidneys was very similar in all three groups (Fig. 4e).

Discussion

In this study, we accomplished visualization of MT1-MMP by MRI using a pre-targeting method with a PAMAM-based contrast agent (Bt-PAMAM-DTPA(Gd)) which possesses high proton relaxivity and high affinity to streptavidin. For future applications, this pre-targeting method based on the interaction between biotin and streptavidin is promising for the detection of functional molecules, such as biomarkers in tumors like MT1-MMP, by *in vivo* MRI.

Although several macromolecular contrast agents have been developed for functional molecular imaging with MRI using a mAb or peptide as the targeting moiety, these attempts have been largely unsuccessful because the macromolecular contrast agents, such as an antibody attached to a dendrimer, have a poorer targeting ability and slower pharmacokinetics in the circulation than the targeting moiety alone, which leads to an inadequately low S/N ratio for several days post-injection [10, 11]. Thus, we focused on a pre-targeting strategy whose effectiveness in elevating the S/N ratio shortly after injection has been well documented in the field of radioimmunotherapy [13, 26]. In the pre-targeting strategy, high affinity between the pre- and post-administered agents is required; thus, the affinity of a post-administered biotinylated contrast agent to streptavidin needed to be evaluated. In this study, Bt-PAMAM-DTPA (Gd) containing approximately ten biotins in the structure showed 43.2- and 1.9-fold higher affinity to streptavidin compared with Bt_1-PAMAM-DTPA(Gd) containing only one biotin per dendrimer and D-biotin, respectively, which suggests a multivalent effect for Bt-PAMAM-DTPA(Gd) binding to streptavidin. Zhu *et al.* recently reported the MRI of functional molecules by a pre-targeting approach [27]; however, the authors failed to show a significant tumor image probably because of the small number of biotins per dendrimer (~4 biotins per dendrimer). Therefore, in a pre-targeting method where a macromolecule is used as the post-administered agent, it is essential that an optimal number of biotins on the macromolecule be evaluated.

In the streptavidin-conjugated anti-MT1-MMP mAb-treated group, MR signals in the tumor and T/M ratios were highly maintained following Bt-PAMAM-DTPA(Gd) administration compared with the saline-treated group, which suggests that the tumor accumulation of Bt-PAMAM-DTPA(Gd) depended on the pre-targeted streptavidin-conjugated anti-MT1-MMP mAb. Furthermore, MR signals in the tumor and T/M ratios were also significantly higher in the streptavidin-conjugated anti-MT1-MMP mAb-treated group than those in the negative control, which suggests that the accumulation of Bt-PAMAM-DTPA(Gd) was primarily specific for MT1-MMP. The slightly significant difference in relative tumor signals for the negative control and saline groups is probably caused in part by passive accumulation of the pre-targeted streptavidin-conjugated antibody as a macromolecule due to an enhanced permeability and retention effect [28].

Previously, to determine the optimal interval between injections of streptavidin-conjugated anti-MT1-MMP mAb and Bt-PAMAM-DTPA(Gd), the biodistribution of ^{125}I-labeled streptavidin-conjugated anti-MT1-MMP mAb was evaluated in C3H/He mice bearing FM3A mouse breast carcinoma [14]. From consideration of the high accumulation of streptavidin-conjugated antibody in the tumor and the high tumor-to-blood ratio at 72 h, we adopted this time as the interval between pre- and post-administrations in this study. Recently, some reports have shown that clearing agents (e.g., galactosylated biotin-albumin conjugate) can readily (within a few hours) clear surplus streptavidin-conjugated antibody from the circulation to the liver where the complex is metabolized and excreted without the loss of biotin binding sites in the tumor [29–31], thereby shortening

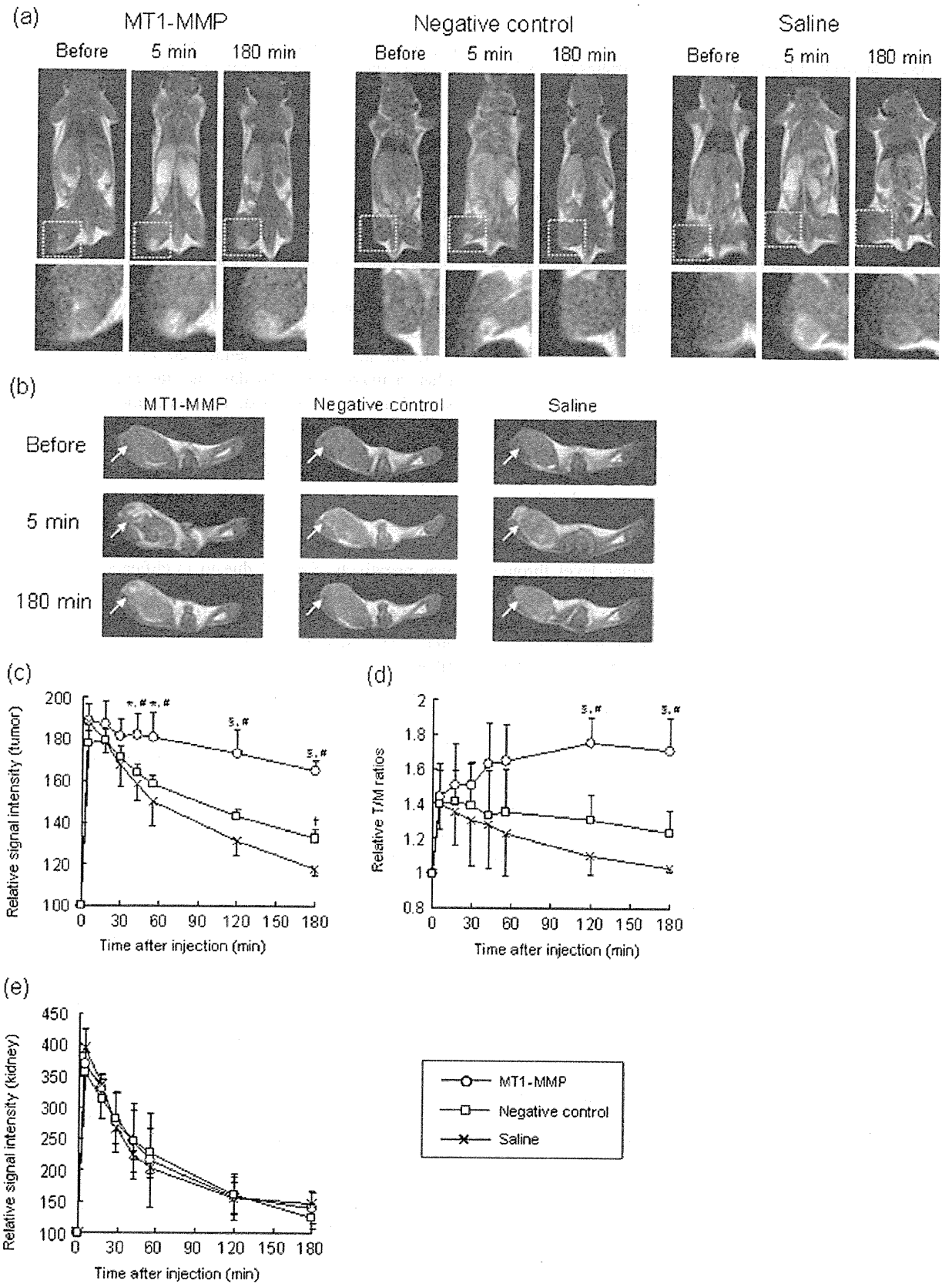

◀ **Fig. 4.** **a**, **b** *In vivo* T_1-weighted MR images of C3H/He mice before and at 5 and 180 min after injection of Bt-PAMAM-DTPA(Gd) following pre-treatment with streptavidin-conjugated anti-MT1-MMP mAb (*MT1-MMP*), streptavidin-conjugated negative control IgG (*Negative control*), or saline (*Saline*). The coronal (**a**) and transaxial (**b**) images are shown. *Arrows* or *dotted squares* indicate the tumor site. Enlarged images of the *dotted square* regions are also shown. **c–e** The dynamic change of signal intensity in the tumor by Bt-PAMAM-DTPA(Gd) (**c**) and relative tumor to muscle ratios (**d**) following pre-treatment with streptavidin-conjugated anti-MT1-MMP mAb (*MT1-MMP*, *circles*), streptavidin-conjugated negative control IgG (*Negative control*, *squares*), or saline (*Saline*, *crosses*). **e** The dynamic change of signal intensity in the kidney for each animal group. **P*<0.05; §*P*<0.01 *vs. Negative control*; #*P*<0.01 *vs. Saline*; †*P*<0.01 *Negative control vs. Saline*.

the interval between injections. In the future, by taking advantage of this type of strategy, we can establish an optimal protocol for MT1-MMP imaging for clinical applications.

Dendrimers are a class of highly branched spherical polymers, with a variety of properties, such as chemical structure, size, molecular weight, and functional groups that can be easily manipulated at the molecular level through their synthesis. The pharmacokinetics of the dendrimer is susceptible to control with its generation number such that it may be highly bioavailable, an important consideration for a variety of applications, especially in the biomedical field [32]. Here, PAMAM dendrimer was chosen as the base structure of the contrast agent for post-administration. PAMAM dendrimer (G4) with an ethylene diamine core has a molecular weight of 14,215 Da and possesses 64 amino groups on the surface of the molecule [33]. In this study, 10 biotins and 44 Gds for specific targeting and sensitive imaging were introduced onto the dendrimer. An *in vitro* MR study showed that the relaxivity of Bt-PAMAM-DTPA(Gd) was 4.3-fold higher than Gd-DTPA, which indicates the effectiveness of Bt-PAMAM-DTPA(Gd) as a contrast agent with high proton relaxivity as expected because of slow tumbling rates and a short water residence time [2, 5].

The post-administered contrast agent in a pre-targeting study should satisfy the following two requirements besides specific affinity to pre-administered streptavidin: rapid blood clearance and low nonspecific accumulation in the tumor. It has been reported that a PAMAM (G4) dendrimer is quickly excreted via glomerular filtration primarily during the first pass (the blood α phase half-life, 2.5 min; β phase half-life, 35 min [34]), and not via the bile pathway. In addition, these dendrimers exhibit no measurable leakage from normal blood vessels because of their moderate size (ca. 6 nm) [2, 34–37], which leads to low nonspecific accumulation in the tumor caused by passive accumulation based on an enhanced permeability and retention effect. PAMAM (G4)-based MR contrast agents can be effective as imaging probes, as supported by the experimental data that showed low MR signals observed in the tumors of the saline pre-targeted group while intense signals were observed in the kidneys after the acute disappearance of Bt-PAMAM-DTPA (Gd) from the circulation.

As mentioned above, in the case of antibody-conjugated dendrimer-based contrast agents, excess antibodies (on the order of milligrams per mouse) are typically administered when injected at a Gd dose (0.1 mmol Gd/kg) necessary for adequate imaging, which leads to major limitations of cost and toxicity. On the other hand, our pre-targeting strategy could control the amount of injected streptavidin-conjugated antibody by corresponding to the targeted molecule (about 50 μg per mouse for MT1-MMP), which would be useful for reducing the cost and toxicity of the imaging process.

In the application of dendrimers *in vivo*, cytotoxicity is often a major issue. To date, as has been widely demonstrated for other polycations, dendrimers bearing amino termini display concentration- and commonly generation-dependent cytotoxicity [38] and potent hemolytic activity [39]. These effects could be attributable to the electrostatic interactions of the positively charged dendrimer with the negatively charged cell membrane under physiological pH. Nevertheless, Bt-PAMAM-DTPA(Gd) used in this study was negatively charged due to modifications of the amino termini to bind biotin and DTPA such that it could be acceptable *in vivo*. This assertion is supported by a report that PAMAM dendrimers bearing carboxylate termini display dramatically lower toxicity to cells [40]. We also plan to acetylate or succinylate the free amino groups to further reduce the positive charge of the complexes if needed to decrease toxicity and hemolytic activity. The rapid excretion of Bt-PAMAM-DTPA(Gd) via glomerular filtration should alleviate adverse effects such as nephrogenic systemic fibrosis [41] derived from released Gd, as compared with macromolecular contrast agents which have slow elimination pharmacokinetics [11, 42], although further analysis of the cytotoxicity is needed.

Conclusions

The pre-targeting method utilizing the specific interaction between streptavidin and biotin enabled the visualization of MT1-MMP expressing tumors by 1.5 T MRI with high S/N ratios during the first hours following administration of a contrast agent, Bt-PAMAM-DTPA(Gd). The results suggest that this method may be beneficial to diagnosing tumor malignancy in a clinical setting. In future work, this method could be applied to the imaging of a variety of pathologic functional molecules expressed on cell surfaces.

Acknowledgments. This study was supported by Grants-in-Aid for Scientific Research and by the 21st Century Center of Excellence Programs at Kyoto University "Knowledge Information Infrastructure for Genome Science" from the Ministry of Education, Culture, Sports, Science and Technology, Japan. A part of this study was conducted as a part of the project "R&D of Molecular Imaging Equipment for Malignant Tumor Therapy Support," supported by the New Energy and Industrial Technology Development Organization (NEDO), Japan.

Conflicts of Interest. The authors have no conflict of interest.

References

1. Caravan P (2006) Strategies for increasing the sensitivity of gadolinium based MRI contrast agents. Chem Soc Rev 35:512–523
2. Kobayashi H, Brechbiel MW (2003) Dendrimer-based macromolecular MRI contrast agents: characteristics and application. Mol Imaging 2:1–10
3. Accardo A, Tesauro D, Roscigno P et al (2004) Physicochemical properties of mixed micellar aggregates containing CCK peptides and Gd complexes designed as tumor specific contrast agents in MRI. J Am Chem Soc 126:3097–3107
4. Mulder WJ, Strijkers GJ, van Tilborg GA, Griffioen AW, Nicolay K (2006) Lipid-based nanoparticles for contrast-enhanced MRI and molecular imaging. NMR Biomed 19:142–164
5. Nicolle GM, Toth E, Schmitt-Willich H, Raduchel B, Merbach AE (2002) The impact of rigidity and water exchange on the relaxivity of a dendritic MRI contrast agent. Chemistry 8:1040–1048
6. Toth EE, Vauthey S, Pubanz D, Merbach AE (1996) Water exchange and rotational dynamics of the dimeric gadolinium(III) complex [BO {Gd(DO3A)(H(2)O)}(2)]: a variable-temperature and -pressure (17)O NMR study(1). Inorg Chem 35:3375–3379
7. Toth E, Merbach AE (1998) Water exchange dynamics: the key for high relaxivity contrast agents in medical magnetic resonance imaging. ACH - Models Chem 135:873–884
8. Sipkins DA, Cheresh DA, Kazemi MR et al (1998) Detection of tumor angiogenesis *in vivo* by alphaVbeta3-targeted magnetic resonance imaging. Nat Med 4:623–626
9. Lee JH, Huh YM, Jun YW et al (2007) Artificially engineered magnetic nanoparticles for ultra-sensitive molecular imaging. Nat Med 13:95–99
10. Boswell CA, Eck PK, Regino CA et al (2008) Synthesis, characterization, and biological evaluation of integrin alphavbeta3-targeted PAMAM dendrimers. Mol Pharm 5:527–539
11. Kobayashi H, Sato N, Saga T et al (2000) Monoclonal antibody-dendrimer conjugates enable radiolabeling of antibody with markedly high specific activity with minimal loss of immunoreactivity. Eur J Nucl Med 27:1334–1339
12. Green NM (1990) Avidin and streptavidin. Meth Enzymol 184:51–67
13. Boerman OC, van Schaijk FG, Oyen WJ, Corstens FH (2003) Pretargeted radioimmunotherapy of cancer: progress step by step. J Nucl Med 44:400–411
14. Sano K, Temma T, Kuge Y et al (2010) Radioimmunodetection of MT1-MMP relevant to tumor malignancy with pre-targeting method. Biol Pharm Bull 32:1589–1595
15. Axworthy DB, Reno JM, Hylarides MD et al (2000) Cure of human carcinoma xenografts by a single dose of pretargeted yttrium-90 with negligible toxicity. Proc Natl Acad Sci USA 97:1802–1807
16. Paganelli G, Malcovati M, Fazio F (1991) Monoclonal antibody pretargetting techniques for tumour localization: the avidin-biotin system. International Workshop on Techniques for Amplification of Tumour Targetting. Nucl Med Commun 12:211–234
17. Goldenberg DM, Sharkey RM, Paganelli G, Barbet J, Chatal JF (2006) Antibody pretargeting advances cancer radioimmunodetection and radioimmunotherapy. J Clin Oncol 24:823–834
18. Sharkey RM, Karacay H, Cardillo TM et al (2005) Improving the delivery of radionuclides for imaging and therapy of cancer using pretargeting methods. Clin Cancer Res 11:7109s–7121s
19. Deryugina EI, Quigley JP (2006) Matrix metalloproteinases and tumor metastasis. Cancer Metastasis Rev 25:9–34
20. Shiomi T, Okada Y (2003) MT1-MMP and MMP-7 in invasion and metastasis of human cancers. Cancer Metastasis Rev 22:145–152
21. Laus S, Sour A, Ruloff R, Toth E, Merbach AE (2005) Rotational dynamics account for pH-dependent relaxivities of PAMAM dendrimeric, Gd-based potential MRI contrast agents. Chemistry 11:3064–3076
22. Foulon CF, Alston KL, Zalutsky MR (1997) Synthesis and preliminary biological evaluation of (3-iodobenzoyl)norbiotinamide and ((5-iodo-3-pyridinyl)carbonyl)norbiotinamide: two radioiodinated biotin conjugates with improved stability. Bioconjug Chem 8:179–186
23. Kudo T, Ueda M, Kuge Y et al (2009) Imaging of HIF-1-active tumor hypoxia using a protein effectively delivered to and specifically stabilized in HIF-1-active tumor cells. J Nucl Med 50:942–949
24. Zhang Y, Wang C, Zhang Y, Sun M (2004) C6 glioma cells retrovirally engineered to express IL-18 and Fas exert FasL-dependent cytotoxicity against glioma formation. Biochem Biophys Res Commun 325:1240–1245
25. Temma T, Sano K, Kuge Y et al (2009) Achievement of MT1-MMP imaging shortly after radioligand administration by pretargeting strategy with SPECT. J Nucl Med 50(suppl):337P
26. Kraeber-Bodere F, Rousseau C, Bodet-Milin C et al (2006) Targeting, toxicity, and efficacy of 2-step, pretargeted radioimmunotherapy using a chimeric bispecific antibody and 131I-labeled bivalent hapten in a phase I optimization clinical trial. J Nucl Med 47:247–255
27. Zhu W, Okollie B, Bhujwalla ZM, Artemov D (2008) PAMAM dendrimer-based contrast agents for MR imaging of Her-2/neu receptors by a three-step pretargeting approach. Magn Reson Med 59:679–685
28. Iyer AK, Khaled G, Fang J, Maeda H (2006) Exploiting the enhanced permeability and retention effect for tumor targeting. Drug Discov Today 11:812–818
29. Pantelias A, Pagel JM, Hedin N et al (2007) Comparative biodistributions of pretargeted radioimmunoconjugates targeting CD20, CD22, and DR molecules on human B-cell lymphomas. Blood 109:4980–4987
30. Sharkey RM, Karacay H, Griffiths GL et al (1997) Development of a streptavidin-anti-carcinoembryonic antigen antibody, radiolabeled biotin pretargeting method for radioimmunotherapy of colorectal cancer. Studies in a human colon cancer xenograft model. Bioconjug Chem 8:595–604
31. Lin Y, Pagel JM, Axworthy D et al (2006) A genetically engineered anti-CD45 single-chain antibody-streptavidin fusion protein for pretargeted radioimmunotherapy of hematologic malignancies. Cancer Res 66:3884–3892
32. Tomalia DA, Reyna LA, Svenson S (2007) Dendrimers as multi-purpose nanodevices for oncology drug delivery and diagnostic imaging. Biochem Soc Trans 35:61–67
33. Tomalia DA, Naylor AM, Goddard WA (1990) Starburst dendrimers: molecular-level control of size, shape, surface chemistry, topology, and flexibility from atoms to macroscopic matter. Angew Chem Int Ed Engl 29:138–175
34. Kobayashi H, Sato N, Hiraga A et al (2001) 3D-micro-MR angiography of mice using macromolecular MR contrast agents with polyamidoamine dendrimer core with reference to their pharmacokinetic properties. Magn Reson Med 45:454–460
35. Sato N, Kobayashi H, Hiraga A et al (2001) Pharmacokinetics and enhancement patterns of macromolecular MR contrast agents with various sizes of polyamidoamine dendrimer cores. Magn Reson Med 46:1169–1173
36. Choyke PL, Kobayashi H (2006) Functional magnetic resonance imaging of the kidney using macromolecular contrast agents. Abdom Imaging 31:224–231
37. Kobayashi H, Brechbiel MW (2005) Nano-sized MRI contrast agents with dendrimer cores. Adv Drug Deliv Rev 57:2271–2286
38. Roberts JC, Bhalgat MK, Zera RT (1996) Preliminary biological evaluation of polyamidoamine (PAMAM) starburst dendrimers. J Biomed Mater Res 30:53–65
39. Malik N, Wiwattanapatapee R, Klopsch R et al (2000) Dendrimers: relationship between structure and biocompatibility *in vitro*, and preliminary studies on the biodistribution of 125I-labelled polyamidoamine dendrimers *in vivo*. J Control Release 65:133–148
40. Jevprasesphant R, Penny J, Jalal R et al (2003) The influence of surface modification on the cytotoxicity of PAMAM dendrimers. Int J Pharm 252:263–266
41. Buhaescu I, Izzedine H (2008) Gadolinium-induced nephrotoxicity. Int J Clin Pract 62:1113–1118
42. Kobayashi H, Kawamoto S, Jo SK et al (2003) Macromolecular MRI contrast agents with small dendrimers: pharmacokinetic differences between sizes and cores. Bioconjug Chem 14:388–394

Arch Toxicol (2011) 85:347–353
DOI 10.1007/s00204-010-0594-9

ORGAN TOXICITY AND MECHANISMS

Ticlopidine-induced hepatotoxicity in a GSH-depleted rat model

Shinji Shimizu · Ryo Atsumi · Tsunenori Nakazawa · Takashi Izumi · Kenichi Sudo · Osamu Okazaki · Hideo Saji

Received: 26 May 2010 / Accepted: 9 September 2010 / Published online: 25 September 2010

Abstract We investigated hepatotoxicity induced by ticlopidine (TIC) in glutathione (GSH)-depleted rats by pre-treatment of a well-known GSH synthesis inhibitor, L-buthionine-S,R-sulfoxinine (BSO). Although sole administration of either TIC or BSO showed no signs of hepatotoxicity, combined administration of TIC with BSO induced hepatotoxicity, which was characterized by centrilobular necrosis of the hepatocytes and an elevation of plasma alanine aminotransferase activity. Administration of radio-labeled TIC in combination with BSO resulted in significantly higher covalent binding to rat liver proteins than that observed after sole dosing of radio-labeled TIC. Pre-treatment of 1-Aminobenzotriazole, a non-specific inhibitor of P450s, completely suppressed both hepatotoxicity and the increased hepatic covalent binding caused by TIC co-treatment with BSO. The results obtained in this animal model suggest that GSH depletion and covalent binding may be involved in hepatotoxicity induced by TIC. These observations may help to understand the risk factors and the mechanism of hepatotoxicity of TIC in humans.

Keywords Ticlopidine · Iidiosyncratic · Hepatotoxicity · Glutathione · Reactive metabolite · Covalent binding

S. Shimizu (✉) · R. Atsumi · T. Nakazawa · T. Izumi · K. Sudo · O. Okazaki
Drug Metabolism and Pharmacokinetics Research Laboratories, Research and Development Division, Daiichi Sankyo Co., Ltd, 1-2-58, Hiromachi, Shinagawa-ku, Tokyo 140-8710, Japan
e-mail: shimizu.shinji.d3@daiichisankyo.co.jp

H. Saji
Department of Patho-Functional Bioanalysis, Graduate School of Pharmaceutical Sciences, Kyoto University, 46-29 Yoshida Shimoadachi-cho, Sakyo-ku, Kyoto 606-8501, Japan

Introduction

Ticlopidine (TIC) is a potent antiplatelet agent (Quinn and Fitzgerald 1999), and the mechanism of action is the irreversible inhibition of the platelet adenosine receptor, P2Y12 (Savi and Herbert 2005; Yoneda et al. 2004). Although it has been widely used for the secondary prevention of atherothrombosis (Jacobson 2004), TIC treatment provokes serious, but rare, adverse events including agranulocytosis (Ono et al. 1991), thrombotic thrombocytopenic purpura (Muszkat et al. 1998; Steinhubl et al. 1999), aplastic anemia (Mataix et al. 1992), and hepatotoxicity (Takikawa 2005). Immune reactions seem to be involved in at least some serious adverse events, such as agranulocytosis (Ono et al. 1991) and hepatic injury (van Zanten and McCormic 1996; Tsai et al. 2000; Hirata et al. 2008). Generally, reactive metabolite formation followed by covalent binding is believed to be associated with idiosyncratic toxicity through the immune mechanism. On the other hand, it was reported that TIC irreversibly modifies proteins in an in vitro study using human liver microsomes and hepatocytes (Ha-Duong et al. 2001; Usui et al. 2009). As a result, we suspected that the reactive metabolites of TIC followed by covalent binding might be responsible for TIC-induced idiosyncratic toxicity.

Since the 1980s, many researchers have utilized glutathione (GSH)-depleted animal as an animal model to underlie the mechanism of hepatotoxicity caused by the reactive metabolites of chemicals, such as butylated hydroxytoluene (Mizutani et al. 1987), eugenol (Mizutani et al. 1991), styrene (Mizutani et al. 1994a), and p-dichlorobenzene (Mizutani et al. 1994b). Additionally, a number of groups, including our group, have applied this GSH-depleted animal model to the evaluation of hepatotoxic potential for several drugs that produce reactive metabolites, for example methimazole

(Mizutani et al. 1999), acetaminophene (Watanabe et al. 2003), tienilic acid (Nishiya et al. 2008), and amodiaquine (Shimizu et al. 2009a). In a GSH-depleted animal system induced by a well-known GSH synthesis inhibitor, L-buthionine-S,R-sulfoxinine (BSO), tissue GSH levels were significantly reduced without any overt toxicity (Watanabe et al. 2003) or any effects on the hepatic microsomal and cytosolic enzymes responsible for the metabolism (Drew and Miners 1984; Watanabe et al. 2003).

The objective of the present study was to investigate the hepatotoxic potential of TIC using a GSH-depleted rat model. Furthermore, the effect of ABT, a non-specific inhibitor of P450, on covalent binding and hepatotoxicity in this GSH-depleted animal was studied in order to elucidate the factors involved in TIC-induced hepatotoxicity. Based on the results of the above studies, we discussed the possible mechanism of hepatotoxicity induced by TIC in humans.

Materials and methods

Chemicals

TIC and BSO were purchased from Wako Pure Chemical Industries, Ltd. (Osaka, Japan). 1-Aminobenzotriazole (ABT) was purchased from Tokyo Chemical Industry Co., Ltd. (Tokyo, Japan). [4-^{14}C]-TIC was obtained from BlyChem Ltd. (Billingham, UK). A DC protein assay kit was purchased from Bio-Rad Laboratories, Inc. (Hercules, CA). All other reagents were of the highest grade commercially available.

Animals

Male Sprague–Dawley rats, 6 or 7 weeks old on the days of the experiment, were obtained from Japan SLC, Inc. (Shizuoka, Japan). The rats were housed at a constant temperature (23 ± 2°C) and humidity (55 ± 10%) under a 12-h light/dark cycle. Except when stated otherwise, the rats received food (FR-2, Funahashi Farm, Chiba, Japan) and water ad libitum.

Assessment of hepatotoxicity

In the time course study, the rats ($n = 4$ for each time point of different dosing groups) were intraperitoneally treated with BSO (700 mg/kg) in water (10 ml/kg). Intraperitoneal dosing of ABT (100 mg/kg) in water (10 ml/kg) was simultaneous with the BSO dosing. One hour later, the rats were orally administered TIC (150 mg/kg) in water (10 ml/kg). Food was removed 14–16 h before BSO dosing and was supplied again 6 h after TIC administration. At 3, 6, 24, and 48 h, blood was collected from the abdominal vena cava, and then the liver was removed under diethyl ether anesthesia. Plasma was separated from these blood samples, and alanine aminotransferase (ALT) was determined with a JCA-BM 2250 automatic analyzer (JEOL Ltd., Tokyo, Japan). A piece of each liver sample was fixed in 10% buffered formalin (Wako Pure Chemical Industries, Ltd.), embedded in paraffin wax, sectioned, and stained with hematoxylin and eosin for the histopathological evaluation. Each remaining liver sample was immediately frozen and stored at −20°C before analysis of the GSH content. In the dose-dependent study, the rats ($n = 6$–9 for each dosage) were intraperitoneally treated with BSO (700 mg/kg), and then 1 h later, they were orally administered TIC at 50, 100, 150, and 300 mg/kg. At 24 h after TIC administration, blood was collected from the abdominal vena cava under diethyl ether anesthesia. Plasma was separated from these blood samples to determine plasma ALT activity.

Assay of hepatic GSH

Liver samples used for the assay of hepatic GSH were basically the ones collected in the time course study on hepatotoxicity. For the control group at 48 h and the BSO/TIC/ABT group at 24 h, four more rats were used. As previously reported (Shimizu et al. 2009a), the hepatic GSH was assessed by determining the acid-soluble non-protein sulfhydryl content (Sedlak and Lindsay 1968), which is mostly comprised of the GSH level in the liver (Ip 1984). Briefly, a piece of each removed liver was weighed and then homogenized with phosphate-buffered saline (pH 7.4). Each resulting homogenate was mixed with 5–15% 5-sulfosalicylic acid, followed by centrifugation (8,000g, 10 min, 4°C). After dilution of each supernatant with distilled water, the GSH level was determined using Total Glutathione Quantification Kit (Dojindo Laboratories, Kumamoto, Japan).

Assay of covalent binding

The rats ($n = 4$ for each time point of different dosing groups) were administered BSO, ABT, and TIC as previously described in the Assessment of hepatotoxicity section with one exception: the use of ^{14}C-TIC (150 mg/kg) in water (10 ml/kg) instead of unlabeled TIC. At 3 and 6 h after ^{14}C-TIC dosing, blood was drawn from the abdominal vena cava, and then the liver was removed under diethyl ether anesthesia. The liver samples were weighed and homogenized with aqueous 1.15% (v/v) KCl. The covalent binding of radioactivity to liver proteins was measured as previously reported (Shimizu et al. 2009a). Briefly, liver homogenate was serially washed with 80% (v/v) aqueous methanol containing 10% (w/v) trichloroacetic acid, diethyl ether–methanol [1:1 (v/v)], and 80% (v/v) aqueous methanol

(twice for each solvent). The resulting precipitated protein was dissolved in 1 N NaOH and then neutralized by adding 5 N HCl. Aliquots were taken for the measurement of the protein content with a DC protein assay kit and for the determination of the radioactivity with a liquid scintillation counter (2300TR, Packard Instruments Company Inc., Palo Alto, CA) and Hionic-fluor scintillation fluid cocktail (PerkinElmer Life and Analytical Sciences, Waltham, MA). The covalent binding of radioactivity to proteins was expressed as the pmol equivalent of ticlopidine/mg of protein.

Statistical analysis

The results of the ALT assay, the GSH assay, and the covalent binding were analyzed by a Dunnett multiple comparison test. SAS System Release 8.2 (SAS Institute Inc., Cary, NC) was used for these statistical analyses.

Results

Assessment of hepatotoxicity

Table 1 shows the time course of rat plasma ALT activities after the administration of TIC in combination with BSO. Sole treatment with either BSO or TIC produced no changes in plasma ALT activities at any time. In contrast, the plasma ALT activity in rats treated with TIC in combination with BSO was significantly increased at 6 h, reached maximum at 24 h, and then slightly decreased at 48 h. Additional treatment of the P450 inhibitor, ABT, completely suppressed the elevation of ALT activity caused by the co-treatment of TIC with BSO. The histopathological evaluation showed vacuolation of the centrilobular hepatocytes at 6 h (Fig. 1a). At 24 h, extensive centrilobular necrosis was observed (Fig. 1b), and then the necrotic change became less abundant at 48 h (Fig. 1c). However, the treatment with BSO or TIC alone or additional treatment of ABT with BSO and TIC (Fig. 1d) had no effect on the liver histology at any time. The dose dependency of the increase in ALT activity was investigated by the combined treatment (Table 2). Although sole administration of TIC showed no increase in ALT activity even at 300 mg/kg, co-treatment of TIC with BSO exhibited tendencies of ALT elevation at 100 mg/kg, and marked elevation was observed at more than 150 mg/kg. Mortality was also observed in a dose-dependent manner at more than 150 mg/kg.

Hepatic GSH level

Figure 2 shows the time course of the hepatic GSH concentration in rats administered TIC in combination with BSO. When the rats were treated with BSO alone, the hepatic GSH was depleted to 9% of the control level at 3 h. The decreased level was maintained by 6 h and then recovered to 52% at 24 h. Treatment of TIC in combination with BSO, independent of the additional dosing of ABT, also showed marked GSH depletion but with a more prolonged depletion (greater depletion even at 24 h) over the sole treatment of BSO. The decreased hepatic GSH was recovered to the control level at 48 h in the ABT-treated rats (given TIC, BSO, and ABT). Meanwhile, hepatic GSH was still significantly reduced even at 48 h in the non-ABT-treated rats (given only TIC and BSO). The hepatic GSH level of the rats receiving TIC alone was also decreased to 43% of the control at 3 h but rebounded to 161% at 6 h and then returned to the control level at 24 h.

Covalent binding of TIC in combination with BSO

Figure 3 shows the covalent binding of TIC to liver proteins with the pre-treatment of BSO or the pre-treatment of both ABT and BSO. Sole administration of TIC showed covalent binding of 648 pmol/mg (6 h) and 473 pmol/mg (24 h), respectively. Combined administration of TIC with

Table 1 Time course of the plasma ALT activities (IU/ml) after administration of ticlopidine (TIC) in combination with L-buthionine-S,R-sulfoxinine (BSO)

Time after TIC (h)	3	6	24	48
Control	31.5 ± 5.4	26.8 ± 7.2	51.3 ± 18.8	51.3 ± 1.5 (n = 3)
BSO	29.3 ± 3.3	34.8 ± 11.0	43.5 ± 4.8	
TIC	32.3 ± 2.1	30.3 ± 3.3	50.0 ± 17.5	
BSO/TIC/ABT	27.5 ± 2.5	31.0 ± 2.2	30.0 ± 2.6[a]	40.5 ± 5.4
BSO/TIC	37.5 ± 8.2	189 ± 183[b]	6,673 ± 2586[c]	2,214 ± 2,895

The rats received TIC (150 mg/kg, p.o.) 1 h after BSO (700 mg/kg, i.p.) and ABT (100 mg/kg, i.p.) dosing (mean ± SD, n = 4)

[a] Significantly different from the BSO/TIC group ($P < 0.001$)

[b] Significantly different from the control group ($P < 0.05$)

[c] Significantly different from the control group ($P < 0.001$)

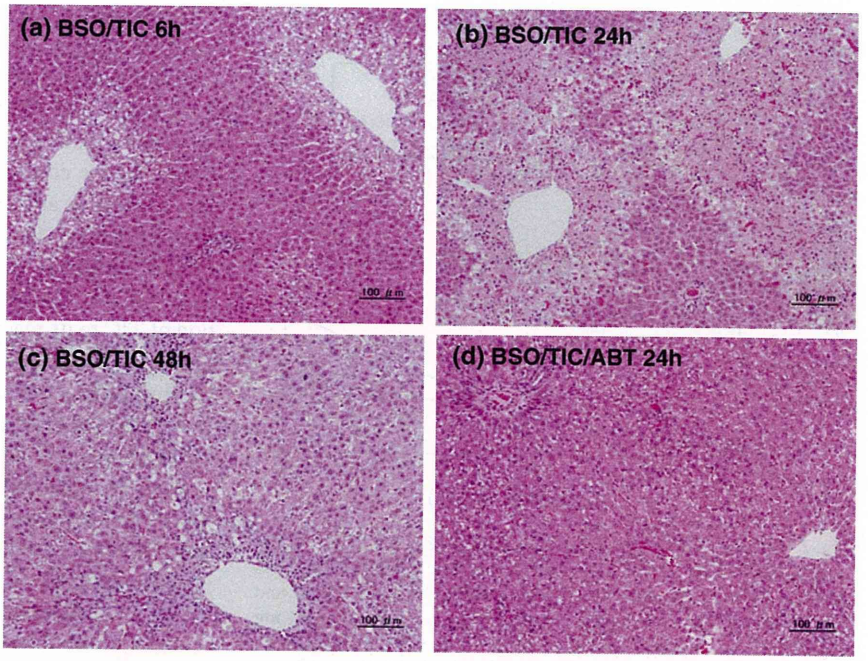

Fig. 1 Histopathological evaluation of the rat liver after administration of ticlopidine (TIC) in combination with L-buthionine-S,R-sulfoxinine (BSO). The liver sections: **a** 6 h, **b** 24 h, and **c** 48 h after administration of TIC (150 mg/kg, p.o.) in combination with BSO (700 mg/kg, i.p.); **d** 24 h after administration of TIC in combination with BSO and ABT (100 mg/kg, i.p.)

Table 2 Dose dependency of the plasma ALT activities (IU/ml) after administration of ticlopidine (TIC) in combination with L-buthionine-S,R-sulfoxinine (BSO)

TIC dose (mg/kg)	50	100	150	300	300 (without BSO)
ALT	80.7 ± 44.7	268 ± 459	3,305 ± 3,079	3,586 ± 2,124	41.0 ± 7.1
Mortality	0/9	0/9	1/9	3/9	0/6

The rats received TIC 1 h after BSO (700 mg/kg, i.p.) dosing (mean ± SD, n = 6–9). Plasma was collected at 24 h after TIC dosing

BSO increased covalent binding by 3.5 times (6 h) and 2.8 times (24 h) more than TIC alone, respectively. Additional treatment of ABT completely prevented the elevation of covalent binding induced by the co-treatment of TIC with BSO at both time points.

Discussion

Oral LD50 for TIC in male rats is 1,780 mg/kg (Panak et al. 1983). No evidence of hepatotoxicity was observed even after repeated administrations of TIC (200 mg/kg, orally) twice daily for 4 days to rats (Panak et al. 1983). In the present study, either administration of TIC alone (150 mg/kg, p.o.) or BSO alone (700 mg/kg, i.p.) to rats showed no sign of hepatotoxicity in terms of plasma ALT activity and liver histopathology (Table 1). In contrast, the administration of TIC in combination with BSO resulted in hepatotoxicity characterized by the elevation of plasma ALT activity and the centrilobular necrosis of hepatocytes (Table 1 and Fig. 1). Dose dependency was observed in the elevation of plasma ALT activity (Table 2). BSO is a specific inhibitor of γ-glutamylcysteine synthetase, a rate-limiting enzyme of GSH synthesis (Griffith and Meister 1979), and can therefore decrease the GSH level even in vivo (Watanabe et al. 2003). In addition, it was reported that BSO has no effect on the content of microsomal cytochrome P450 and the activity of conjugating enzymes, such as GSH S-transferase, sulfotransferase, and UDP-glucuronosyltransferase (Drew and Miners 1984; Watanabe et al. 2003). Therefore, GSH depletion is likely to cause hepatotoxicity in rats treated with TIC at doses of 150 and 300 mg/kg. Administration of radio-labeled TIC in combination with BSO caused significantly higher covalent binding of radioactivity to rat liver than that observed after sole dosing of radio-labeled TIC (Fig. 3). This is consistent with the previous in vitro finding in which covalent binding of TIC in the absence of GSH was threefold higher than that with GSH after incubation with human recombinant P450 (Ha-Duong et al. 2001). TIC produces reactive metabolites, including reactive thiophene-S-oxide and epoxide in liver microsomes, which are either scavenged by GSH or covalently bind to proteins (Ha-Duong et al. 2001; Ruan and Zhu 2010; Shimizu et al. 2009b). These findings presumably suggest that in

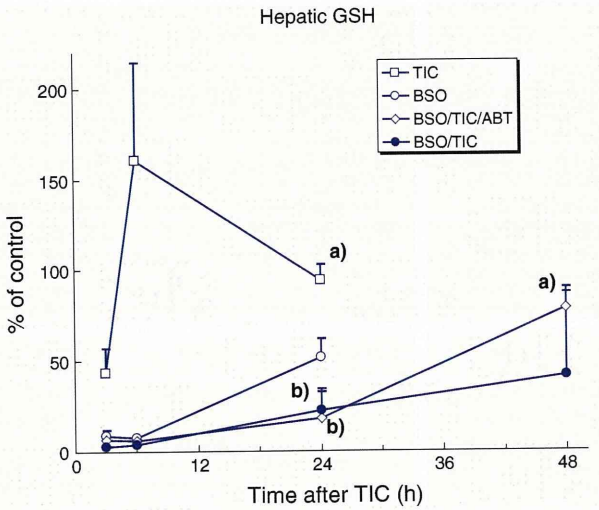

Fig. 2 Hepatic GSH level after administration of ticlopidine (TIC) in combination with L-buthionine-S,R-sulfoxinine (BSO). The rats received TIC (150 mg/kg, p.o.) 1 h after BSO (700 mg/kg, i.p.) and ABT (100 mg/kg, i.p.) dosing (mean + SD, $n = 4$–8). Values are expressed as a percentage of the control group. **a** NOT significantly different from the control group ($P \geq 0.05$). **b** Significantly different from both control group and BSO group ($P < 0.05$). The control values of the GSH level (μmol/g liver) for 3, 6, 24, and 48 h were 1.59 ± 0.37, 1.23 ± 0.24, 6.14 ± 1.46, and 5.11 ± 1.21, respectively

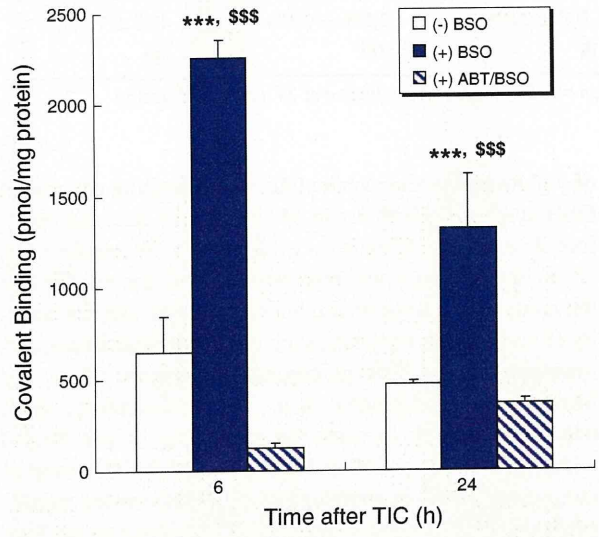

Fig. 3 Covalent binding to the liver after administration of ^{14}C-ticlopidine (TIC) in combination with buthionine-S,R-sulfoxinine (BSO). Rats received ^{14}C-TIC (150 mg/kg, p.o.) 1 h after BSO (700 mg/kg, i.p.) and ABT (100 mg/kg, i.p.) dosing (mean + SD, $n = 4$). ***$P <$ 0.001: Significantly different from the (−) BSO group. $$$$P < 0.001$: Significantly different from the (+) ABT/BSO group

GSH-depleted rats, an insufficient detoxication reaction of reactive intermediates of TIC with GSH followed by an increased level of covalent binding to proteins might finally result in hepatotoxicity.

Additionally, we investigated the effect of ABT, a non-specific inhibitor of P450 s, on the hepatotoxicity and the covalent binding observed in this GSH-depleted animal. Pre-treatment of ABT completely suppressed both the hepatotoxicity and the increased hepatic covalent binding caused by the co-treatment of TIC with BSO (Table 1 and Fig. 3) without any effect on GSH depletion (at least up to 24 h post-dose, Fig. 2). ABT is known to diminish the in vivo oxidative drug metabolism of P450 without any overt toxicity (Mugford et al. 1992). Moreover, bioactivation of TIC to its reactive metabolites is reported to be mediated by P450 (Ha-Duong et al. 2001). Thus, covalent binding (derived from P450-dependent formation of reactive metabolites) as well as GSH level may be involved in the hepatotoxicity induced by TIC.

Hepatic GSH was also decreased after sole administration of TIC at 3 h post-dose (Fig. 2). A similar hepatic GSH reduction was observed for several drugs, such as acetaminophene (Mitchell et al. 1973), tienilic acid (Nishiya et al. 2008), and amodiaquine (Shimizu et al. 2009a), which form reactive metabolites. The decreased hepatic GSH induced by the combined administration of TIC with BSO was recovered to the control level at 48 h in ABT-treated rats (given TIC, BSO, and ABT), but not recovered in non-ABT-treated rats (given only TIC and BSO). This is presumably due to the hepatic damage induced by the combined treatment of TIC with BSO rather than the inhibition of GSH synthesis caused by BSO. In fact, this GSH depletion in non-ABT-treated rats was well correlated with the ALT increase in the 4 individual animals (105, 53, 2, and 6% of the control GSH level vs. 586, 516, 6530, and 1,224 IU/ml of plasma ALT activity, respectively).

According to previous papers reporting TIC-induced hepatotoxicity in humans, more than half of the cases were cholestasis, and the rest of them were the hepatocellular-type or mixed-type damage (Hirata et al. 2008; Mizushima et al. 2005; Pizarro et al. 2001). However, this might not be entirely consistent with the present rat study where only hepatocellular-type damage (centrilobular necrosis) was observed. On the contrary, Takikawa (2005) stated in his review article that, in one of the reported studies, all of the cases with suspected hepatotoxicity due to TIC were the hepatocellular type with a mild increase in ALT and that such a slight increase in ALT in humans may be transient. This might partly explain the difference in the hepatic damage pattern between our "single-dose study" in animals, where only hepatocellular-type damage was observed, and the reported "chronic surveys" in humans, where cholestasis and mixed-type damage were also observed.

Idiosyncratic toxicity appears to be associated with multiple determinants such as environmental and genetic factors of patients, as well as the exposure level of the chemical itself (Li 2002). In clinical situations, the GSH

level is decreased with factors such as aging (Hernanz et al. 2000), alcoholics (Lauterburg and Velez 1988), and HIV infection (Staal et al. 1992) or is affected by dietary nutrition including cysteine (Micke et al. 2002) and vitamin B6 (Davis et al. 2006). Moreover, genetic polymorphism of glutamate-cysteine ligase, a rate-limiting enzyme for GSH synthesis, is related to the plasma GSH content (Nakamura et al. 2002). In addition to the GSH level, as to the amount of TIC covalent binding, CYP2C19 was shown to be involved in adduct formation (Ha-Duong et al. 2001). Moreover, CYP2B6 was reported to be time-dependently inhibited by TIC (Richter et al. 2004; Nishiya et al. 2009), indicating that CYP2B6 would also be associated with covalent binding through the reactive intermediates formed by CYP2B6 itself. Both CYP2C19 and CYP2B6 are genetically polymorphic, and their allelic variants are known to result in altered enzymatic activities (Zhou et al. 2009). Therefore, genetic polymorphism of these CYP isozymes could be related to the formation of TIC adducts. Although the relevance between the GSH content, CYP polymorphism, and TIC-induced hepatotoxicity in humans remains to be investigated, some patients with multiple factors as described above might have a reduced intracellular GSH level and/or increased CYP activity level sufficient to evoke liver damage. Thus, our results showing hepatotoxicity and covalent binding of TIC in GSH-depleted rats might provide a possible mechanism for the idiosyncratic hepatotoxicity of TIC observed in humans.

In conclusion, we investigated hepatotoxicity induced by TIC using a GSH-depleted rat model. The present study revealed that TIC reproduces hepatotoxicity in this animal model and demonstrated that this hepatotoxicity is related to the hepatic GSH level and covalent binding. These observations may help us to understand the risk factors and the mechanism of hepatotoxicity of TIC in humans.

Acknowledgments We would like to thank Minoru Inoue and Yutaka Iigo for their excellent assistance with the histopathological evaluations. We are also very grateful to Takatoshi Nishiya for his helpful comments.

References

Davis SR, Quinlivan EP, Stacpoole PW, Gregory JF III (2006) Plasma glutathione and cystathionine concentrations are elevated but cysteine flux is unchanged by dietary vitamin B-6 restriction in young men and women. J Nutr 136:373–378

Drew R, Miners JO (1984) The effects of buthionine sulfoximine (BSO) on glutathione depletion and xenobiotic biotransformation. Biochem Pharmacolo 33:2989–2994

Griffith OW, Meister A (1979) Potent and specific inhibition of glutathione synthesis by buthionine sulfoximine (S-n-butyl homocysteine sulfoximine). J Biol Chem 254:7558–7560

Ha-Duong NT, Dijols S, Macherey AC, Goldstein JA, Dansette PM, Mansuy D (2001) Ticlopidine as a selective mechanism-based inhibitor of human cytochrome P450 2C19. Biochemistry 40:12112–12122

Hernanz A, Fernández-Vivancos E, Montiel C, Vazquez JJ, Arnalich F (2000) Changes in the intracellular homocysteine and glutathione content associated with aging. Life Sci 67:1317–1324

Hirata K, Takagi H, Yamamoto M, Matsumoto T, Nishiya T, Mori K, Shimizu S, Masumoto H, Okutani Y (2008) Ticlopidine-induced hepatotoxicity is associated with specific human leukocyte antigen genomic subtypes in Japanese patients: a preliminary case-control study. Pharmacogenomics J 8:29–33

Ip C (1984) Comparative effects of antioxidants on enzymes involved in glutathione metabolism. Life Sci 34:2501–2506

Jacobson AK (2004) Platelet ADP receptor antagonists: ticlopidine and clopidogrel. Best Pract Res Clin Haematol 17:55–64

Lauterburg BH, Velez ME (1988) Glutathione deficiency in alcoholics: risk factor for paracetamol hepatotoxicity. Gut 2:1153–1157

Li AP (2002) A review of the common properties of drugs with idiosyncratic hepatotoxicity and the "multiple determinant hypothesis" for the manifestation of idiosyncratic drug toxicity. Chem Biol Interact 142:7–23

Mataix R, Ojeda E, Perez MC, Jimenez S (1992) Ticlopidine and severe aplastic anaemia. Br J Haematol 80:125–126

Micke P, Beeh KM, Buhl R (2002) Effects of long-term supplementation with whey proteins on plasma glutathione levels of HIV-infected patients. Eur J Nutr 4:12–18

Mitchell JR, Jollow DJ, Potter WZ, Gillette JR, Brodie BB (1973) Acetaminophene-induced hepatic necrosis. IV. Protective role of glutathione. J Pharmacol Exp Ther 187:211–217

Mizushima M, Iwata N, Fujimoto TT, Ishikawa K, Fujimura K (2005) Patient characteristics in ticlopidine hydrochloride-induced liver injury: Case-control study. Hepatol Res 33:234–240

Mizutani T, Nomura H, Nakanishi K, Fujita S (1987) Hepatotoxicity of butylated hydroxytoluene and its analogs in mice depleted of hepatic glutathione. Toxicol Appl Pharmacol 87:166–176

Mizutani T, Satoh K, Nomura H, Nakanishi K (1991) Hepatotoxicity of eugenol in mice depleted of glutathione by treatment with DL-buthionine sulfoximine. Res Commun Chem Pathol Pharmacol 71:219–230

Mizutani T, Irie Y, Nakanishi K (1994a) Styrene-induced hepatotoxicity in mice depleted of glutahione. Res Commun Mol Pathol Pharmacol 86:361–374

Mizutani T, Nakahori Y, Yamamoto K (1994b) p-Dichlorobenzene-induced hepatotoxicity in mice depleted of glutathione treated with buthionine sulfoximine. Toxicology 94:57–67

Mizutani T, Murakami M, Shirai M, Tanaka M, Nakanishi K (1999) Metabolism-dependent hepatotoxicity of Methimazole in mice depleted of glutathione. J Appl Toxicol 19:193–198

Mugford CA, Mortillo M, Mico BA, Tarloff JB (1992) 1-Aminobenzotriazole-induced destruction of hepatic and renal cytochromes P450 in male Sprague-Dawley rats. Fundam Appl Toxicol 19:43–49

Muszkat M, Shapira MY, Sviri S, Linton DM, Caraco Y (1998) Ticlopidine-induced thrombotic thrombocytopenic purpura. Pharmacotherapy 18:1352–1355

Nakamura S, Kugiyama K, Sugiyama S, Miyamoto S, Koide S, Fukushima H, Honda O, Yoshimura M, Ogawa H (2002) Polymorphism in the 5′-flanking region of human glutamate-cysteine ligase modifier subunit gene is associated with myocardial infarction. Circulation 105:2968–2973

Nishiya T, Mori K, Hattori C, Kai K, Kataoka H, Masubuchi N, Jindo T, Manabe S (2008) The crucial protective role of glutathione against tienilic acid hepatotoxicity in rats. Toxicol Appl Pharmacol 232:280–291

Nishiya Y, Hagihara K, Ito T, Tajima M, Miura S, Kurihara A, Farid NA, Ikeda T (2009) Mechanism-based inhibition of human cytochrome P450 2B6 by ticlopidine, clopidogrel, and the thiolactone metabolite of prasugrel. Drug Metab Dispos 37:589–593

Ono K, Kurohara K, Yoshihara M, Shimamoto Y, Yamaguchi M (1991) Agranulocytosis caused by ticlopidine and its mechanism. Am J Hematol 37:239–242

Panak E, Maffrand JP, Picard-Fraire C, Vallée E, Blanchard J, Roncucci R (1983) Ticlopidine: a promise for the prevention and treatment of thrombosis and its complications. Haemostasis 13(Suppl 1):1–54

Pizarro AE, Andrade RJ, García-Cortés M, Lucena MI, Pérez-Moreno JM, Puertas M, Sánchez-Martínez H, Montero JL, Durán JA, Jiménez M, Ruiz-Montero A, Soto-Conesa MJ, Rodrigo L, de Francisco R, Alcántara R, Camargo R (2001) Acute hepatitis due to ticlopidine. A report of 12 cases and review of the literature. Rev Neurol 33:1014–1020

Quinn MJ, Fitzgerald DJ (1999) Ticlopidine and clopidogrel. Circulation 100:1667–1672

Richter T, Mürdter TE, Heinkele G, Pleiss J, Tatzel S, Schwab M, Eichelbaum M, Zanger UM (2004) Potent mechanism-based inhibition of human CYP2B6 by clopidogrel and ticlopidine. J Pharmacol Exp Ther 308:189–197

Ruan Q, Zhu M (2010) Investigation of Bioactivation of Ticlopidine Using Linear Ion Trap/Orbitrap Mass Spectrometry and an Improved Mass Defect Filtering Technique. Chem Res Toxicol 23:909–917

Savi P, Herbert JM (2005) Clopidogrel and ticlopidine: P2Y12 adenosine diphosphate-receptor antagonists for the prevention of atherothrombosis. Semin Thromb Hemost 31:174–183

Sedlak J, Lindsay RH (1968) Estimation of total, protein-bound, and nonprotein sulfhydryl groups in tissue with Ellman's reagent. Anal Biochem 25:192–205

Shimizu S, Atsumi R, Itokawa K, Iwasaki M, Aoki T, Ono C, Izumi T, Sudo K, Okazaki O (2009a) Metabolism-dependent hepatotoxicity of amodiaquine in glutathione-depleted mice. Arch Toxicol 83:701–707

Shimizu S, Atsumi R, Nakazawa T, Fujimaki Y, Sudo K, Okazaki O (2009b) Metabolism of ticlopidine in rats: Identification of the main biliary metabolite as a GSH conjugate of S-oxide. Drug Metab Dispos 37:1904–1915

Staal FJ, Ela SW, Roederer M, Anderson MT, Herzenberg LA (1992) Glutathione deficiency and human immunodeficiency virus infection. Lancet 339:909–912

Steinhubl SR, Tan WA, Foody JM, Topol EJ (1999) Incidence and clinical course of thrombotic thrombocytopenic purpura due to ticlopidine following coronary stenting. EPISTENT Investigators. Evaluation of Platelet IIb/IIIa Inhibitor for Stenting. JAMA 281:806–810

Takikawa H (2005) Lessons from ticlopidine-induced liver injury. Hepatol Res 33:193–194

Tsai MH, Tsai SL, Chen TC, Liaw YF (2000) Ticlopidine-induced cholestatic hepatitis with anti-nuclear antibody in serum. J Formos Med Assoc 99:866–869

Usui T, Mise M, Hashizume T, Yabuki M, Komuro S (2009) Evaluation of the potential for drug-induced liver injury based on in vitro covalent binding to human liver proteins. Drug Metab Dispos 37:2383–2392

van Zanten SV, McCormic CW (1996) Antinuclear antibody-positive ticlopidine-induced hepatitis. Can J Gastroenterol 10:231–232

Watanabe T, Sagisaka H, Arakawa S, Shibaya Y, Watanabe M, Igarashi I, Tanaka K, Totsuka S, Takasaki W, Manabe S (2003) A novel model of continuous depletion of glutathione in mice treated with L-buthionine (S, R)-sulfoximine. J Toxicol Science 28:455–463

Yoneda K, Iwamura R, Kishi H, Mizukami Y, Mogami K, Kobayashi S (2004) Identification of the active metabolite of ticlopidine from rat in vitro metabolites. Br J Pharmacol 142:551–557

Zhou SF, Liu JP, Chowbay B (2009) Polymorphism of human cytochrome P450 enzymes and its clinical impact. Drug Metab Rev 41:89–295

MOLECULAR IMAGING AND BIOLOGY

Published Online: 14 September 2010

Mol Imaging Biol (2011) 13:1003–1010
DOI: 10.1007/s11307-010-0418-6

RESEARCH ARTICLE

PET Imaging of Hypoxia-Inducible Factor-1-Active Tumor Cells with Pretargeted Oxygen-Dependent Degradable Streptavidin and a Novel ^{18}F-Labeled Biotin Derivative

Takashi Kudo,[1] Masashi Ueda,[1,2] Hiroaki Konishi,[1] Hidekazu Kawashima,[1,3] Yuji Kuge,[1,4] Takahiro Mukai,[5] Azusa Miyano,[1] Shotaro Tanaka,[6] Shinae Kizaka-Kondoh,[6] Masahiro Hiraoka,[6] Hideo Saji[1]

[1]*Department of Patho-Functional Bioanalysis, Graduate School of Pharmaceutical Sciences, Kyoto University, 46-29 Yoshida Shimoadachi-cho, Sakyo-ku, Kyoto 606-8501, Japan*
[2]*Radioisotopes Research Laboratory, Kyoto University Hospital, Faculty of Medicine, Kyoto University, Kyoto 606-8507, Japan*
[3]*Department of Nuclear Medicine and Diagnostic Imaging, Graduate School of Medicine, Kyoto University, Kyoto 606-8507, Japan*
[4]*Central Institute of Isotope Science, Hokkaido University, Sapporo 060-0815, Japan*
[5]*Department of Biomolecular Recognition Chemistry, Graduate School of Pharmaceutical Sciences, Kyushu University, Fukuoka 812-8582, Japan*
[6]*Department of Radiation Oncology and Image-Applied Therapy, Graduate School of Medicine, Kyoto University, Kyoto 606-8507, Japan*

Abstract

Purpose: We aimed to evaluate the feasibility of using streptavidin–biotin-based pretargeting for positron emission tomography (PET) imaging of hypoxia-inducible factor (HIF)-1-active tumors.

Procedures: We used POS, a genetically engineered form of streptavidin that selectively stabilizes in HIF-1-active cells, and (4-^{18}F-fluorobenzoyl)norbiotinamide (^{18}F-FBB), a radiolabeled biotin derivative, for performing a biodistribution study and for PET imaging. The tumoral ^{18}F-FBB accumulation was compared to the HIF-1-dependent luciferase bioluminescence and HIF-1α immunohistochemical signal.

Results: ^{18}F-FBB accumulation was observed in POS-pretargeted tumors in mice (2.85±0.55% injected dose per gram at 3 h), and clear PET images were obtained at the same time point. The tumoral ^{18}F-FBB accumulation positively correlated with luciferase bioluminescence (R=0.72, P<0.05), and most of the area showing ^{18}F-FBB accumulation corresponded to HIF-1α-positive areas.

Conclusion: Pretargeting with POS and ^{18}F-FBB is an effective approach for PET imaging of HIF-1-active areas in tumors.

Key Words: Tumor hypoxia, Hypoxia-inducible factor-1 (HIF-1), Oxygen-dependent degradation domain (ODD), Pretargeting, ^{18}F-labeled biotin derivative

Introduction

Abnormal rapid growth of tumor cells outstrips the blood supply, which develops an oxygen tension below physiologic levels (hypoxia) [1]. It appears to be strongly

Electronic supplementary material The online version of this article (doi:10.1007/s11307-010-0418-6) contains supplementary material, which is available to authorized users.

Correspondence to: Hideo Saji; *e-mail:* hsaji@pharm.kyoto-u.ac.jp

associated with malignant progression and the development of radioresistance [2, 3]. The transcription factor hypoxia-inducible factor-1 (HIF-1) has been reported to be one of the critical components of hypoxic responses [4]. Because HIF-1 was recently reported to be closely related to tumor malignancy and to hinder both chemotherapy and radiation therapy [5, 6], noninvasive imaging of HIF-1-active hypoxic tumor cells may be useful in making a qualitative diagnosis and establishing a therapy for cancer. The oxygen-sensitive alpha subunit of HIF-1 (HIF-1α) contains an oxygen-dependent degradation domain (ODD) and regulates the HIF-1 activity by inducing the degradation of HIF-1 via the ODD under normoxic conditions [7]. Therefore, it is likely that a probe that contains the ODD and induces degradation in a similar manner as HIF-1α does can be used to evaluate HIF-1 activity *in vivo*.

We have recently synthesized proteins in which the protein transduction domain (PTD) is fused to the ODD and demonstrated that these proteins were efficiently delivered to hypoxic regions and were stabilized in HIF-1-active cells [8–11]. We have also fused the PTD and the ODD with monomeric streptavidin (SAV) to produce a chimeric protein, PTD-ODD-SAV (POS), and synthesized a radiolabeled biotin derivative, (3-$^{123/125}$I-iodobenzoyl)norbiotinamide ($^{123/125}$I-IBB). POS was degraded in an oxygen-dependent manner, and a clear image of the tumor was obtained at 24 h after the injection of ^{123}I-IBB-conjugated POS. The accumulation of ^{123}I-IBB-conjugated POS in the tumor was found to correlate with the HIF-1 activity [12]. Furthermore, we were able to obtain the tumor image rapidly by using a pretargeting approach. An adequate-contrast image was obtained just 6 h after injection of ^{123}I-IBB in the pretargeting approach, while 24 h was required when using ^{123}I-IBB-conjugated POS [13].

Compared to single-photon emission computed tomography imaging, positron emission tomography (PET) imaging is more sensitive and quantitative, and provides images with a higher spatial resolution. The limited and heterogeneous expression of HIF-1 in the tumor necessitated a high-spatial-resolution device for the accurate imaging of HIF-1-expressed regions. Therefore, we attempted to obtain PET images of the HIF-1-active hypoxic tumors by using POS. Since a period of 24 h was required to obtain an adequate-contrast image by using directly radiolabeled POS [12], we adopted the pretargeting approach to reduce radiation exposure.

Fluorine-18 is one of the most widely used positron emitters because of its adequate half-life, ease of production, and low positron energy; hence, a ^{18}F-labeled biotin derivative may be useful in PET imaging. However, there have been few reports of the application of such a molecule in pretargeted imaging [14]. Therefore, we synthesized (4-^{18}F-fluorobenzoyl)norbiotinamide (^{18}F-FBB) in order to perform PET studies with POS. This study aimed to evaluate the feasibility of using POS and ^{18}F-FBB for pretargeted PET imaging of HIF-1-active areas in tumors.

Materials and Methods

Synthesis of $^{18/19}$F-FBB

N-Succinimidyl-4-fluorobenzoate (SFB, compound 2) was synthesized according to a previously described method [15]. The detailed method of FBB (compound 3) synthesis has been described in the supplemental materials (Online Resource 1).

The synthesis of ^{18}F-FBB (^{18}F-3) is outlined in Fig. 1. Fluorine-18 was produced via the ^{18}O(p,n)^{18}F nuclear reaction by using a proton beam current to irradiate ^{18}O-H_2O [16, 17]. ^{18}F-SFB (^{18}F-2) was synthesized according to a previously described method [18, 19] and obtained with decay-uncorrected radiochemical yield of 30–40%. ^{18}F-SFB was then concentrated under a stream of nitrogen and added to a solution of *N*,*N*′-dimethylformamide (DMF)/water (4:1); the DMF solution contained norbiotinamine hydrochloride (5 mg/mL). NEt_3 was added to make the solution basic. The reaction was performed at room temperature for 0.5–1 h, and the reaction mixture was loaded onto a C18 Sep-Pak cartridge (Waters, Milford, MA, USA). The C18 cartridge was eluted with water and then with acetonitrile. The acetonitrile fraction was evaporated, and the residue was purified using high performance liquid chromatography (HPLC) (Cosmosil 5C_{18}MS-II column; Nacalai Tesque, Kyoto, Japan; 25% acetonitrile; flow rate, 1 mL/min). The retention time of ^{18}F-FBB was 11 min. The radiochemical purity was measured using HPLC, and the specific activity was determined on the basis of the ultraviolet absorbance at 254 nm. The solvent was removed by rotary evaporation and reconstituted in water or saline for use in *in vitro* and *in vivo* studies.

Preparation of Fusion Protein

POS was overexpressed in *Escherichia coli* and purified as described in a previous report [12]. Purified POS was dissolved in Tris–HCl buffer (pH 8.0).

Binding of POS and ^{18}F-FBB

^{18}F-FBB, D-biotin (0–500 pmol), and POS (0.04 pmol) were mixed and incubated in 100 mM citrate buffer (pH 5.0) for 1 h at 37°C. The binding of ^{18}F-FBB to POS in the absence of D-biotin was detected using size-exclusion chromatography (PD-10; GE Healthcare Bioscience, Uppsala, Sweden). The reaction mixture containing D-biotin was applied to an Amicon Microcon filter (Millipore) and centrifuged at 4,500×*g* for 30 min at 4°C (Micro Cooling Centrifuge 1720; Kubota, Osaka, Japan). The radioactivities of the reactant and filtrate (unbound ^{18}F-FBB) were measured, and the binding rate was calculated. All measurements were performed in triplicate.

Cell and Cell Culture

FM3A mouse mammary tumor cells were purchased from Health Science Research Resources Bank (Osaka, Japan). Suit2 human pancreatic tumor cells were originally obtained from the American Type Culture Collection (Manassas, VA, USA). Suit2/5HRE-

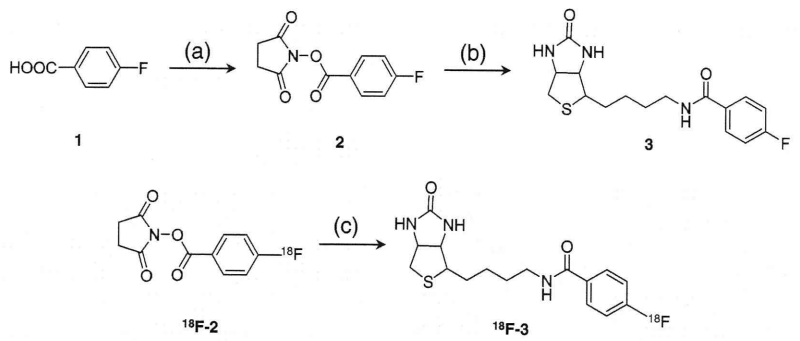

Fig. 1. Synthesis of FBB (3) and ^{18}F-FBB (^{18}F-3). (a) *N,N,N',N'*-Tetramethyl-*O*-(*N*-succinimidyl)uranium tetrafluoroborate, CH_3CN, 90°C, 10 h. (b) Norbiotinamine, NEt_3, DMF/H_2O (4:1), r.t., 5 h. (c) Norbiotinamine, NEt_3, DMF/H_2O (4:1), r.t., 1 h.

CMV_{mp}-Luciferase (Suit2/Luc) cells that express luciferase in response to HIF-1 activity were established and supplied by Prof. Kizaka-Kondoh [20]. Both cell types were cultured using a previously reported method [12, 13].

Animal Model

Animal studies were conducted in accordance with our institutional guidelines, and the experimental procedures were approved by the Kyoto University Animal Care Committee. Female C3H/He mice and BALB/c *nu/nu* mice at 5 weeks of age were purchased from Japan SLC, Inc. (Hamamatsu, Japan). Models of FM3A and Suit2/Luc tumors were prepared as described in a previous report [12]. After tumor implantation, mice were fed an AIN76-A-based, biotin-free diet (Oriental Yeast Co. Ltd., Tokyo, Japan) in order to prevent dietary biotin from inhibiting the binding of ^{18}F-FBB to POS. The mice were subjected to a tracer study at 2–3 weeks after the implantation. The average diameter and average volume of the tumors were approximately 10 mm and 500 mm^3, respectively.

Biodistribution

^{18}F-FBB (370 kBq) was injected intravenously into FM3A-implanted mice (n=4–5); the mice were sacrificed at 0.5, 1, 3, and 6 h after the injection. For the pretargeting study, we used the protocol that has been previously reported as an optimal method [13]. The mice (n=4–5) were intravenously injected with 30 μg of POS; after 24 h, ^{18}F-FBB (370 kBq) was injected intravenously. The mice were sacrificed at the same time points as mentioned above. Whole organs were immediately obtained and weighed, and their radioactivity was measured. The results were expressed in terms of the percent injected dose per gram of tissue (%ID/g).

In Vivo Blocking Study

FM3A-implanted mice (n=4) were pretargeted with POS (30 μg); after 23.5 h, the mice were injected with a vehicle or saline solution of D-biotin (1 nmol). After another 30 min, ^{18}F-FBB (370 kBq) was administered and 3 h later, the mice were sacrificed. Whole organs were immediately removed and weighed, and their radioactivity was measured. The results were expressed as %ID/g.

^{18}F-FBB Accumulation vs. HIF-1 Transcriptional Activity in Tumors in Mice Pretargeted with POS

Some Suit2/Luc-implanted mice (n=8) were pretargeted with 30 μg of POS. After 24 h, ^{18}F-FBB (370 kBq for five mice and 18.5 MBq for three mice) was administered intravenously. For immunohistochemical analysis, the mice that received the higher dose of ^{18}F-FBB were intraperitoneally injected with pimonidazole (PIMO, 60 mg/kg) 1 h after the ^{18}F-FBB injection. Further, 2.5 h after the ^{18}F-FBB injection, 200 μL of D-luciferin solution (10 mg/mL in PBS; VivoGlo Luciferin, Promega, WI, USA) was injected intraperitoneally. After 20 min, the mice were anesthetized with 2.5% isoflurane, and bioluminescence imaging was performed using IVIS Spectrum System (Xenogen, Alameda, CA, USA). The signal intensity within the tumors was analyzed using Living Image 3.0 software (Xenogen). The mice were sacrificed 3 h after the ^{18}F-FBB injection, the radioactivity of the tumors was measured, and the results were expressed in terms of %ID. The tumor specimens obtained from the mice injected with the higher dose of ^{18}F-FBB were subjected to an autoradiographic study.

Another set of Suit2/Luc-implanted mice (n=4) were pretargeted with 30 μg of POS. After 24 h, ^{18}F-FBB (18.5 MBq) was administered intravenously and 6 h later, the bioluminescence signal and radioactivity were compared using the procedure described above. After the radioactivity measurement, the tumor specimens were subjected to metabolite analysis.

Size-Exclusion Analysis of Radioactive Compounds in Tumors

After bioluminescence imaging, each mouse was anesthetized with 2.5% isoflurane, and urine was collected from its bladder. The mice were then sacrificed, and their tumors were immediately removed. Extracts were prepared using a previously reported method [13], with a slight modification. In brief, the tumors were homogenized in ice-cold 0.1 M Tris–HCl buffer containing 1% sodium dodecyl sulfate and 0.15 M NaCl (pH 6.5), by using a Polytron homogenizer (PT10-35; Kinematica AG, Switzerland). The preparations were then centrifuged at 4°C and 4,600×g for 20 min. The

supernatants and urine were analyzed by size-exclusion chromatography with a PD-10 column.

Autoradiography

Autoradiographic studies were performed on the same mice used for the bioluminescence imaging (n=3). Ten-micrometer-thick frozen tumor sections were prepared according to a previously reported procedure [21]. The sections were exposed to imaging plates (BAS-SR; Fuji Photo Film Co., Ltd., Tokyo, Japan) for 3 h, and autoradiograms were then obtained and analyzed as previously described [21], except that BAS5000 was used instead of BAS3000 (both scanners, Fuji Photo Film Co., Ltd.).

Immunohistochemical Analysis

The adjacent 10-μm-thick sections used in the autoradiographic study were subjected to dual fluorescent immunostaining for HIF-1α and PIMO according to a previously described method [13]. In brief, the sections were fixed, blocked, and treated with anti-human/mouse HIF-1α polyclonal antibody (R&D Systems, Minneapolis, MN, USA), as a primary antibody. The specific signals were detected using an Alexa Fluor 568-conjugated $F(ab')_2$ fragment of goat anti-rabbit antibody (Invitrogen, San Diego, CA, USA). Thereafter, the sections were washed with PBS and treated with fluorescein isothiocyanate-conjugated mouse IgG_1 monoclonal antibody (Chemicon, Temecula, CA, USA) according to the manufacturer's protocol for PIMO staining. The sections were then dried and coverslipped using an antifade reagent (ProLong Gold with DAPI; Invitrogen). Another adjacent section was stained with hematoxylin–eosin (HE). Fluorescent and bright-field microscopic images were obtained using BIOREVO BZ-9000 (Keyence Corp., Osaka, Japan).

PET Imaging

^{18}F-FBB (22.2±6.7 MBq) was injected into the tail veins of FM3A-implanted mice (n=6) 24 h after they were pretargeted with POS (30 μg). The mice were anesthetized with 2.5% isoflurane and placed on a scanner bed in the prone position. At 3 h after the injection, the mice were imaged for 15 min by using eXplore VISTA (GE Healthcare Bioscience). An energy window of 250–700 keV was used. Before reconstruction, the raw data were corrected for random and scattered coincidences, and radioactive decay. Attenuation correction was not performed. PET images were reconstructed according to a standard filtered back-projection procedure (FBP) with a Ramp filter (alpha, 1.0; cutoff, 1.0) or by using a two-dimensional ordered-subset expectation maximization algorithm (2D-OSEM; iterations, 2; subsets, 16). The regions of interest were drawn on the tumor and the corresponding area in the left thigh of the FBP-reconstructed images.

Statistical Analyses

The two groups were compared using the Mann–Whitney U test, and correlation coefficients were assessed using the Spearman rank analysis. Values of $P<0.05$ were considered statistically significant.

Results

Radiosynthesis of ^{18}F-FBB

The decay-uncorrected radiochemical yield from ^{18}F-SFB as a starting material was 38%; radiochemical purity, >95%; total synthesis time, 70–100 min; and specific activity at the end of synthesis, >97 GBq/μmol (limit of detection).

Binding of POS and ^{18}F-FBB

After the incubation of ^{18}F-FBB with POS, the radioactivity was detected at macromolecular fraction, as determined using size-exclusion chromatography; this indicated that ^{18}F-FBB bound to POS (data not shown). The binding of ^{18}F-FBB to POS was not inhibited by D-biotin at concentrations <100 nM (binding rate, 99.7±0.2%), whereas it was completely inhibited by 1,000 nM D-biotin (binding rate, 6.0±1.3%); the results of inhibition study are similar to those using ^{18}F-FBB alone (5.5±0.5%), *i.e.*, in the case of non-specific absorption to the column (Fig. 2).

Biodistribution

An examination of the biodistribution of ^{18}F-FBB alone revealed that both the tumor-to-blood and the tumor-to-

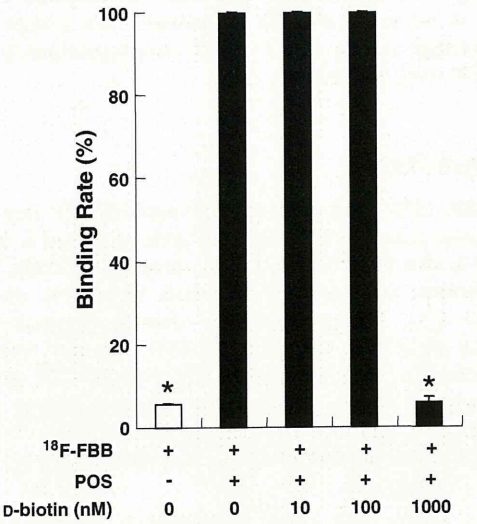

Fig. 2. Binding of ^{18}F-FBB to POS. The *black columns* represent the mean calculated binding rate of ^{18}F-FBB and POS in the presence of various concentrations of D-biotin. The *white column* represents the calculated binding rate of ^{18}F-FBB alone, which indicates non-specific absorption to the column. D-biotin (1,000 nM) significantly inhibited ^{18}F-FBB binding to POS compared to the binding in the other D-biotin-treated group (*P<0.05).

Table 1. Biodistribution of ^{18}F-FBB in FM3A-implanted mice

Organ	Time after injection (h)			
	0.5	1	3	6
Blood	1.68±0.19	0.86±0.12	0.10±0.07	0.04±0.01
Liver	12.07±1.11	7.30±1.24	0.44±0.06	0.24±0.11
Kidney	10.19±1.14	6.42±0.75	0.42±0.07	0.24±0.12
Intestine	17.99±1.92	21.12±7.27	7.72±1.15	3.72±1.81
Tumor	1.38±0.60	0.77±0.29	0.11±0.10	0.05±0.03
Muscle	2.08±0.23	1.70±0.74	0.09±0.06	0.13±0.08
Bone	1.14±0.96	1.54±0.52	0.27±0.20	0.20±0.17
Tumor/blood	0.83±0.39	0.90±0.30	0.64±0.20	0.94±0.30
Tumor/muscle	0.66±0.26	0.66±0.71	0.95±0.61	0.36±0.37

Organ uptake values are expressed as the percent injected dose per gram of tissue, except in the case of the tumor/blood and tumor/muscle ratios. Values are represented as the mean±SD. n=4–5

muscle ratios were less than 1 at all time points. This indicated that ^{18}F-FBB did not accumulate in the tumors. Moreover, ^{18}F-FBB was rapidly cleared from all organs, except the intestine (Table 1). In contrast, in the pretargeted group, tumor accumulation of ^{18}F-FBB 3 h after injection was 2.85±0.55% ID/g, which was more than 20-fold than for ^{18}F-FBB alone (0.11±0.10% ID/g) (Table 2). The tumor-to-blood and tumor-to-muscle ratios were greater than 1 as early as 30 min after the injection, and both these ratios increased in a time-dependent manner because of the rapid clearance of ^{18}F-FBB from the body. Although ^{18}F-FBB accumulation in the kidneys and intestine was high, the radioactivity in the other normal tissues showed a more rapid decrease than in the tumor (Table 2). Pretreatment with D-biotin markedly decreased ^{18}F-FBB accumulation (80%) in the tumors (Table 3). The ^{18}F-FBB accumulation in the other tissues also decreased following treatment with D-biotin.

^{18}F-FBB Accumulation vs. HIF-1 Transcriptional Activity in Tumors in Mice Pretargeted with POS

A significant positive correlation was observed between HIF-1-induced luciferase bioluminescence and ^{18}F-FBB accumulation 3 h after injection in tumors in mice pretargeted with POS (R=0.72, P<0.05; Fig. 3). A similar correlation was also observed at 6 h after the injection (R=0.70, P<0.05, data not shown).

Table 2. Biodistribution of ^{18}F-FBB in FM3A-implanted mice pretargeted with POS

Organ	Time after injection (h)			
	0.5	1	3	6
Blood	2.79±0.57	1.54±0.47	0.56±0.16	0.57±0.22
Liver	15.02±2.05	12.69±1.86	5.74±1.18	3.76±0.51
Kidney	21.59±3.24	19.52±2.71	9.22±1.92	4.87±0.99
Intestine	12.68±2.60	13.68±2.52	5.95±1.57	1.64±0.51
Tumor	4.65±0.49	4.70±0.97	2.85±0.55	2.48±0.49
Muscle	2.49±0.71	2.55±1.21	0.93±0.40	0.29±0.15
Bone	2.82±0.26	3.92±2.42	1.27±0.42	0.91±0.22
Tumor/blood	1.73±0.47	3.16±0.59	5.36±1.32	4.91±2.04
Tumor/muscle	1.98±0.54	2.18±0.75	3.93±2.50	9.51±3.31

Organ uptake values are expressed as the percent injected dose per gram of tissue, except in the case of the tumor/blood and tumor/muscle ratios. Values are represented as the mean±SD. n=4–5

Table 3. Blocking study of the biodistribution of ^{18}F-FBB in FM3A-implanted mice pretargeted with POS

Organ	Vehicle	D-biotin pretreatment
Blood	0.66±0.06	0.22±0.10*
Liver	3.58±1.00	1.48±0.67*
Kidney	3.39±1.05	0.80±0.41*
Intestine	6.59±2.76	7.90±0.98
Tumor	2.06±0.29	0.34±0.14*
Muscle	0.28±0.04	0.14±0.06*
Bone	1.50±1.37	1.31±0.38
Tumor/blood	4.00±2.38	1.63±0.19*
Tumor/muscle	7.29±0.94	2.53±1.19**

Organ uptake values are expressed as the percent injected dose per gram of tissue, except in the case of the tumor/blood and tumor/muscle ratios. Values are represented as the mean±SD. n=4
*P<0.05, **P<0.01 vs. vehicle group

Size-Exclusion Analysis of Radioactive Compounds in Tumors

The recovery of radioactivity from the tumor samples was 94±7.4%, and that from the PD-10 columns was 98±14%. A major proportion of the radioactivity was eluted in a macromolecular fraction (79±5.8%, n=4).

Urine analysis was performed using two samples because the quantity of urine obtained from two mice was too small. In the case of the urine samples, the recovery of radioactivity from the PD-10 columns was 92% and 99%. More than 99% of the radioactivity of both samples was eluted in a small-molecule fraction.

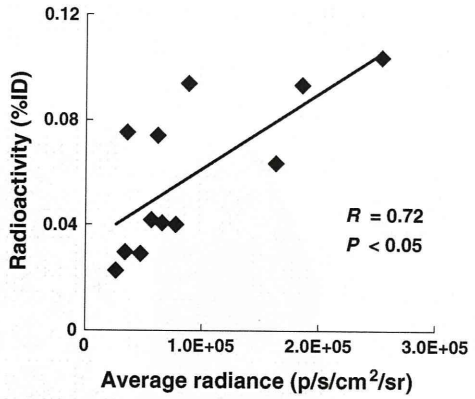

Fig. 3. Correlation between the ^{18}F-FBB accumulation at 3 h post-injection and HIF-1 activity within a tumor pretargeted with POS. The ordinate represents accumulated radioactivity (%ID), and the abscissa represents HIF-1-induced luciferase bioluminescence. The correlation coefficient (R) was 0.72, indicating a highly significant correlation (P<0.05).

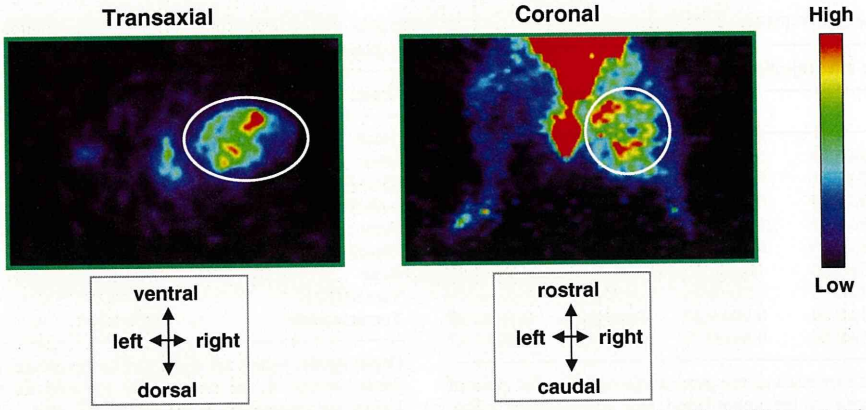

Fig. 4. Typical PET images of FM3A-implanted mice. The mice were pretargeted with POS, and 24 h later, they were intravenously injected with ^{18}F-FBB. Images were acquired 3 h after the ^{18}F-FBB injection and reconstructed using 2D-OSEM. Tumors can be clearly visualized in both images (*circle*).

PET Imaging

The high-resolution PET imaging of the mice clearly showed the tumors implanted in the right thigh (Fig. 4). The calculated tumor-to-muscle ratio was 3.4±1.4.

Histology, Autoradiography, and Immunohistochemistry

HE staining revealed the presence of necrotic areas in the tumor (Fig. 5a). PIMO-positive areas were located in the center of the section, surrounding the necrotic core (Fig. 5b), whereas HIF-1α-positive areas were present peripherally (Fig. 5c). The autoradiogram showed that the distribution of ^{18}F-FBB in the POS-pretargeted tumor was heterogeneous (Fig. 5d). Most of the ^{18}F-FBB-accumulated areas corresponded to the HIF-1α-positive areas. These findings were similar for each tumor examined in this study.

Discussion

The most important aspect of the present study was to evaluate whether the accumulation of ^{18}F-FBB in POS-pretargeted tumors reflects the level of HIF-1 expression or activity. For this purpose, we compared ^{18}F-FBB accumulation with HIF-1 transcriptional activity and HIF-1 immunohistochemical signal among tumors in the same animals that expressed the HIF-1-dependent luciferase reporter gene. In the tumors in the mice pretargeted with POS, the accumulated radioactivity at both 3 and 6 h after the administration of ^{18}F-FBB significantly correlated with the luciferase bioluminescence, *i.e.*, the HIF-1 activity. Furthermore, the tumor-to-blood ratios at 3 and 6 h were also similar. On the basis of these results, we performed the PET-imaging study at 3 h after the injection of ^{18}F-FBB because imaging in the early phase after probe injection is preferred in order to avoid radioactive decay and to reduce radiation exposure. The PET images showed the heterogeneous intratumoral distribution of ^{18}F-FBB in the mice pretargeted

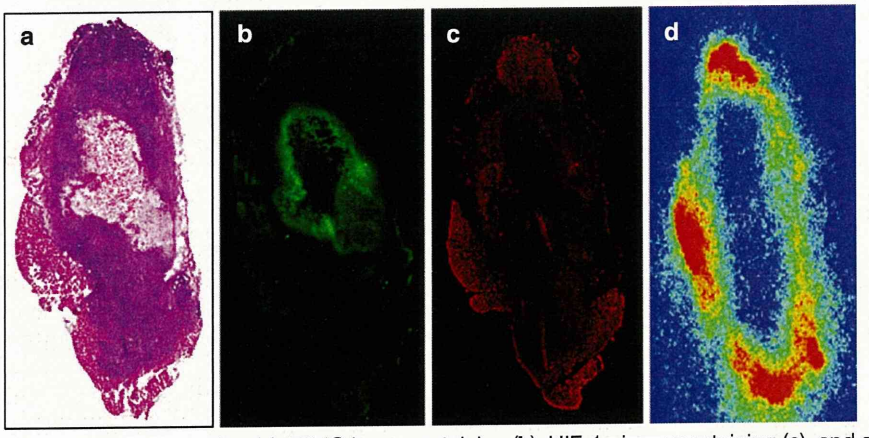

Fig. 5. Representative images of HE staining (**a**), PIMO immunostaining (**b**), HIF-1α immunostaining (**c**), and autoradiography (**d**).

with POS; this result would reflect the HIF-1-active regions because the intratumoral HIF-1-active regions have been reported to be heterogeneous [22]. In fact, the majority of ^{18}F-FBB-accumulated areas corresponded to the HIF-1α-positive areas observed on autoradiography. Therefore, these findings indicate that PET imaging with POS pretargeting and the use of ^{18}F-FBB can help detect intratumoral HIF-1-active regions. These findings are in accordance with those of our previous study where ^{123}I-IBB was used instead of ^{18}F-FBB [13]. Because the lipophilicity of ^{18}F-FBB is lower than that of ^{123}I-IBB, ^{18}F-FBB showed faster blood clearance and a higher tumor-to-blood ratio within a short duration after the injection.

Some hypoxia-imaging probes—such as ^{18}F-fluoromisonidazole (^{18}F-FMISO), 1-α-D-(5-deoxy-5-^{18}F-fluoroarabinofuranosyl)-2-nitroimidazole (^{18}F-FAZA), and ^{64}Cu-diacetyl-bis(N^4-methylthiosemicarbazone) (^{64}Cu-ATSM)—have been developed [23, 24]. These probes can detect low oxygen pressures (less than 10 mmHg) and are useful in predicting the efficacy of radiotherapy [25]. In the present study, the distribution pattern of ^{18}F-FBB in the POS-pretargeted tumor was different from that in the PIMO-positive areas. This result is somewhat different from that obtained in our previous studies where ^{125}I-IBB, which was used in the pretargeting study, and ^{125}I-IPOS were mainly distributed near the PIMO-positive areas [12, 13]. One reason for this discordant result may be the difference in the tumor models used. Suit2 pancreatic tumor cells were used for the autoradiographic and histological analyses in the present study, whereas MDA-MB-231 mammary tumor cells were used in the case of the ^{125}I-IPOS study [12]. Another reason could be the difference in tumor size. The tumor volume used in the present study was approximately 1.5 times greater than that used in the ^{125}I-IBB study [13]. In fact, even with the same tumor model, similarity between the distribution patterns of HIF-1α- and PIMO-positive areas depended on the tumor size; these areas were adjacently located in small tumors but had a different distribution pattern in large tumors [26]. Oh *et al.* reported that ^{64}Cu-ATSM accumulated on the surface of the tumor, whereas PIMO-positive areas located in the center [27]. This finding is similar to that obtained in the present study on ^{18}F-FBB distribution patterns in POS-pretargeted tumors; however, the researchers have not determined HIF-1α expression in the tumor model used in their study. A direct comparison between the POS/^{18}F-FBB system and other hypoxia-imaging probes will help to clarify the differences in the characteristics of the tumor cells that existed in each area where probe accumulation was observed, and in the information obtained from each image.

The basic requirements of an effective biotin derivative for the pretargeting approach include stability against metabolism *in vivo*, rapid clearance from the circulation, and a binding affinity to (strept)avidin. The first-generation radiolabeled biotin derivatives were easily degraded by biotinidase [28]. Biotinidase-mediated degradation can be stopped by creating a reversed amide bond (*i.e.*, NH–CO bond) between the valeryl chain of biotin and the prosthetic group [29]. On the basis of these reports, we decided to convert the terminal carboxylic group of biotin into a primary amine. We found that ^{18}F-FBB stably existed in mouse plasma (data shown in the supplemental materials, Online Resource 2), indicating that this compound was resistant to degradation by biotinidase. The results of the biodistribution study revealed that the accumulated radioactivity in the bone was low and that it did not increase in a time-dependent manner. These results suggest that ^{18}F-FBB is resistant to defluorination *in vivo*. Furthermore, ^{18}F-FBB was rapidly cleared from the blood. ^{18}F-FBB bound to POS and the binding was inhibited by D-biotin both *in vitro* and *in vivo*. These results indicate that ^{18}F-FBB meets the basic requirements of an effective biotin derivative for use in the pretargeting approach.

We found that ^{18}F-FBB accumulated in the POS-pretargeted tumors. Further, this accumulation was inhibited by D-biotin, and a major proportion of the radioactivity of the tumor was attributable to macromolecules. Taken together, these results indicate that the intratumoral radioactivity was caused by the binding of ^{18}F-FBB to the SAV moiety of POS. Thus, we concluded that ^{18}F-FBB can bind streptavidin not only *in vitro* but also *in vivo*. The amount of ^{18}F-FBB accumulation in the tumor was not as high as that of ^{18}F-FDG [30]; this finding could have been due to the limited expression of HIF-1. The expression of HIF-1 is not ubiquitous, but heterogeneous, and is small in tumors [31]. In fact, radioligand accumulation in tumors harboring HIF-1-dependent reporter genes has been reported to range from 1% to 2% ID/g in previous studies [31–33]. Furthermore, the amount of ^{18}F-FBB accumulation was similar to that of other hypoxia-imaging probes such as ^{18}F-FMISO and ^{64}Cu-ATSM (2–5% ID/g) [30, 34, 35].

In the pretargeted group, some abdominal organs showed higher radioactivity accumulation than the tumor. The high background activity in the abdominal region hampers the evaluation of the HIF-1 activity in the abdomen and pelvis, and further modification is required for such an evaluation. The radioactivity of the liver and kidneys may be attributable to the high accumulation of POS in these tissues [12]. Pretreatment of D-biotin decreased ^{18}F-FBB accumulation in the liver and kidneys, suggesting that not all the POS in these tissues was degraded or cleared within 24 h. The slow rate of degradation is a drawback of using POS. Optimization of the interval between the POS and ^{18}F-FBB administration is necessary when imaging HIF-1-active regions in the liver and kidneys. On the other hand, the radioactivity in the intestine was not blocked by D-biotin pretreatment. It is reported that biotinidase, which is involved in the transport of biotin, exists in the intestine [36]. Thus, radioactivity accumulation in the intestine would reflect the behavior of ^{18}F-FBB itself, and not its binding to POS. In this case, the biotin derivatives that show faster clearance from the body [37] may be effective agents.

Conclusion

We have developed a novel radiolabeled biotin derivative, ^{18}F-FBB, and confirmed its ability to bind to the streptavidin moiety both *in vitro* and *in vivo*. ^{18}F-FBB accumulated in the tumors pretargeted with POS; these tumors were clearly visualized on PET imaging. The accumulation of ^{18}F-FBB significantly correlated with the HIF-1 transcriptional activity, and the intratumoral distribution of ^{18}F-FBB corresponded to HIF-1α-positive areas in the tumors pretargeted with POS. These findings suggest that POS and ^{18}F-FBB are potent probes for the PET imaging of HIF-1-active areas in tumors.

Acknowledgments. We are grateful to Hiroyuki Kimura, Kenji Tomatsu, and Yu Ogawa for preparation of ^{18}F-SFB, and Kei Ogawa for skilled technical assistance.

This study was supported in part by Health Labour Sciences Research Grant for Research on Advanced Medical Technology from the Ministry of Health, Labour and Welfare of Japan; "R&D of Molecular Imaging Equipment for Malignant Tumor Therapy Support" by the New Energy and Industrial Technology Development Organization (NEDO), Japan; and a Grant-in-Aid for Exploratory Research (17659010) and a Grant-in-Aid for Young Scientists (B) (21791187) from the Ministry of Education, Culture, Sports, Science and Technology of Japan.

Conflict of interest. The authors have no conflict of interest.

References

1. Vaupel P, Kallinowski F, Okunieff P (1989) Blood flow, oxygen and nutrient supply, and metabolic microenvironment of human tumors: a review. Cancer Res 49:6449–6465
2. Brown JM (2000) Exploiting the hypoxic cancer cell: mechanisms and therapeutic strategies. Mol Med Today 6:157–162
3. Hockel M, Vaupel P (2001) Tumor hypoxia: definitions and current clinical, biologic, and molecular aspects. J Natl Cancer Inst 93:266–276
4. Semenza GL (2007) Life with oxygen. Science 318:62–64
5. Semenza GL (2003) Targeting HIF-1 for cancer therapy. Nat Rev Cancer 3:721–732
6. Dewhirst MW, Cao Y, Moeller B (2008) Cycling hypoxia and free radicals regulate angiogenesis and radiotherapy response. Nat Rev Cancer 8:425–437
7. Wang GL, Jiang BH, Rue EA, Semenza GL (1995) Hypoxia-inducible factor 1 is a basic-helix-loop-helix-PAS heterodimer regulated by cellular O_2 tension. Proc Natl Acad Sci U S A 92:5510–5514
8. Harada H, Kizaka-Kondoh S, Li G et al (2007) Significance of HIF-1-active cells in angiogenesis and radioresistance. Oncogene 26:7508–7516
9. Harada H, Kizaka-Kondoh S, Hiraoka M (2005) Optical imaging of tumor hypoxia and evaluation of efficacy of a hypoxia-targeting drug in living animals. Mol Imaging 4:182–193
10. Kizaka-Kondoh S, Konse-Nagasawa H (2009) Significance of nitroimidazole compounds and hypoxia-inducible factor-1 for imaging tumor hypoxia. Cancer Sci 100:1366–1373
11. Kizaka-Kondoh S, Tanaka S, Harada H, Hiraoka M (2009) The HIF-1-active microenvironment: an environmental target for cancer therapy. Adv Drug Deliv Rev 61:623–632
12. Kudo T, Ueda M, Kuge Y et al (2009) Imaging of HIF-1-active tumor hypoxia using a protein effectively delivered to and specifically stabilized in HIF-1-active tumor cells. J Nucl Med 50:942–949
13. Ueda M, Kudo T, Kuge Y et al (2010) Rapid detection of hypoxia-inducible factor-1-active tumours: pretargeted imaging with a protein degrading in a mechanism similar to hypoxia-inducible factor-1α. Eur J Nucl Med Mol Imaging 37:1566–1574
14. Shoup TM, Fischman AJ, Jaywook S, Babich JW, Strauss HW, Elmaleh DR (1994) Synthesis of fluorine-18-labeled biotin derivatives: biodistribution and infection localization. J Nucl Med 35:1685–1690
15. Vaidyanathan G, Zalutsky MR (2006) Synthesis of N-succinimidyl 4-[^{18}F]fluorobenzoate, an agent for labeling proteins and peptides with ^{18}F. Nat Protoc 1:1655–1661
16. Hara T, Higashi T, Nakamoto Y et al (2009) Significance of chronic marked hyperglycemia on FDG-PET: is it really problematic for clinical oncologic imaging? Ann Nucl Med 23:657–669
17. Ono M, Watanabe R, Kawashima H et al (2009) Fluoro-pegylated chalcones as positron emission tomography probes for *in vivo* imaging of beta-amyloid plaques in Alzheimer's disease. J Med Chem 52:6394–6401
18. Kimura H, Tomatsu K, Kawashima H et al (2009) Development of one-flow synthesis method for N-succinimidyl 4-[F-18]fluorobenzoate ([F-18]SFB) using microreactor for 3-step-reaction. J Label Compd Radiopharm 52:S9–S9
19. Tang G, Zeng WB, Yu MX, Kabalka G (2008) Facile synthesis of N-succinimidyl 4-[F-18]fluorobenzoate ([F-18]SFB) for protein labeling. J Label Compd Radiopharm 51:68–71
20. Kizaka-Kondoh S, Itasaka S, Zeng L et al (2009) Selective killing of hypoxia-inducible factor-1-active cells improves survival in a mouse model of invasive and metastatic pancreatic cancer. Clin Cancer Res 15:3433–3441
21. Ueda M, Iida Y, Tominaga A et al (2010) Nicotinic acetylcholine receptors expressed in the ventralposterolateral thalamic nucleus play an important role in anti-allodynic effects. Br J Pharmacol 159:1201–1210
22. Picchio M, Beck R, Haubner R et al (2008) Intratumoral spatial distribution of hypoxia and angiogenesis assessed by ^{18}F-FAZA and ^{125}I-Gluco-RGD autoradiography. J Nucl Med 49:597–605
23. Krohn KA, Link JM, Mason RP (2008) Molecular imaging of hypoxia. J Nucl Med 49 Suppl 2:129S–148S
24. Mees G, Dierckx R, Vangestel C, Van de Wiele C (2009) Molecular imaging of hypoxia with radiolabelled agents. Eur J Nucl Med Mol Imaging 36:1674–1686
25. Dunphy MP, Lewis JS (2009) Radiopharmaceuticals in preclinical and clinical development for monitoring of therapy with PET. J Nucl Med 50 Suppl 1:106S–121S
26. Lehmann S, Stiehl DP, Honer M et al (2009) Longitudinal and multimodal *in vivo* imaging of tumor hypoxia and its downstream molecular events. Proc Natl Acad Sci U S A 106:14004–14009
27. Oh M, Tanaka T, Kobayashi M et al (2009) Radio-copper-labeled Cu-ATSM: an indicator of quiescent but clonogenic cells under mild hypoxia in a Lewis lung carcinoma model. Nucl Med Biol 36:419–426
28. Chauhan J, Dakshinamurti K (1986) Purification and characterization of human serum biotinidase. J Biol Chem 261:4268–4275
29. Foulon CF, Alston KL, Zalutsky MR (1997) Synthesis and preliminary biological evaluation of (3-iodobenzoyl)norbiotinamide and ((5-iodo-3-pyridinyl)carbonyl)norbiotinamide: two radioiodinated biotin conjugates with improved stability. Bioconjug Chem 8:179–186
30. Liu RS, Chou TK, Chang CH et al (2009) Biodistribution, pharmacokinetics and PET imaging of [^{18}F]FMISO, [^{18}F]FDG and [^{18}F]FAc in a sarcoma- and inflammation-bearing mouse model. Nucl Med Biol 36:305–312
31. Serganova I, Doubrovin M, Vider J et al (2004) Molecular imaging of temporal dynamics and spatial heterogeneity of hypoxia-inducible factor-1 signal transduction activity in tumors in living mice. Cancer Res 64:6101–6108
32. Hsieh CH, Kuo JW, Lee YJ, Chang CW, Gelovani JG, Liu RS (2009) Construction of mutant TKGFP for real-time imaging of temporal dynamics of HIF-1 signal transduction activity mediated by hypoxia and reoxygenation in tumors in living mice. J Nucl Med 50:2049–2057
33. Wen B, Burgman P, Zanzonico P et al (2004) A preclinical model for noninvasive imaging of hypoxia-induced gene expression; comparison with an exogenous marker of tumor hypoxia. Eur J Nucl Med Mol Imaging 31:1530–1538
34. Lewis JS, McCarthy DW, McCarthy TJ, Fujibayashi Y, Welch MJ (1999) Evaluation of ^{64}Cu-ATSM *in vitro* and *in vivo* in a hypoxic tumor model. J Nucl Med 40:177–183
35. Piert M, Machulla HJ, Picchio M et al (2005) Hypoxia-specific tumor imaging with ^{18}F-fluoroazomycin arabinoside. J Nucl Med 46:106–113
36. Dakshinamurti K, Chauhan J, Ebrahim H (1987) Intestinal absorption of biotin and biocytin in the rat. Biosci Rep 7:667–673
37. Hainsworth J, Harrison P, Mather SJ (2005) Preparation and characterization of a DOTA–lysine–biotin conjugate as an effector molecule for pretargeted radionuclide therapy. Bioconjug Chem 16:1468–1474